



HAL
open science

Nonsmooth modal analysis of an elastic bar subject to a unilateral contact constraint

Carlos Yoong, Anders Thorin, Mathias Legrand

► **To cite this version:**

Carlos Yoong, Anders Thorin, Mathias Legrand. Nonsmooth modal analysis of an elastic bar subject to a unilateral contact constraint . 2017. hal-01471341v1

HAL Id: hal-01471341

<https://hal.science/hal-01471341v1>

Preprint submitted on 9 Mar 2017 (v1), last revised 21 Jan 2018 (v2)

HAL is a multi-disciplinary open access archive for the deposit and dissemination of scientific research documents, whether they are published or not. The documents may come from teaching and research institutions in France or abroad, or from public or private research centers.

L'archive ouverte pluridisciplinaire **HAL**, est destinée au dépôt et à la diffusion de documents scientifiques de niveau recherche, publiés ou non, émanant des établissements d'enseignement et de recherche français ou étrangers, des laboratoires publics ou privés.



Distributed under a Creative Commons Attribution 4.0 International License

Nonsmooth modal analysis of an elastic bar subject to a unilateral contact constraint

Carlos Yoong, Anders Thorin, Mathias Legrand

McGill University, 845 Sherbrooke West Street, Montréal, Québec, Canada

Abstract

This contribution proposes a numerical procedure capable of performing nonsmooth modal analysis (mode shapes and corresponding frequencies) of the autonomous wave equation defined on a finite one-dimensional domain with one end subject to a Dirichlet condition and the other end subject to a frictionless time-independent unilateral contact condition. *Nonsmooth modes of vibration* are defined as one-parameter continuous families of nonsmooth periodic orbits satisfying the equation of the dynamics together with the unilateral contact condition. The analysis is achieved using the Wave Finite Element Method, which is a shock-capturing Finite Volume method. As opposed to the traditional Finite Element Method with time-stepping schemes, potentially discontinuous deformation, stress and velocity wave fronts induced by the contact condition are here accurately described, which is critical for seeking periodic orbits. Additionally, the proposed strategy neither introduces numerical dispersion nor artificial dissipation of energy, as required for modal analysis. As a consequence of the mixed time–space discretization, no impact law is required for the well-posedness of the problem in line with the continuous framework.

The frequency–energy dependency—shown as *backbone curves*—provides valuable insight of the system where intricate dynamics such as internal resonance or subharmonic vibration emerges. In contrast to the linear system (without the unilateral contact condition) whose modes are standing harmonic waves, the found autonomous periodic solutions are traveling waves induced by the contact constraints. It is also shown that the periodically-forced vibratory resonances of the system with light structural damping are well predicted by nonsmooth modal analysis. As expected, the open-gap and prestressed configurations at rest show stiffening and softening behaviors respectively.

Keywords: wave propagation, nonsmooth dynamics, unilateral contact, modal analysis, nonlinear vibration, internal resonance

1. Introduction

Exploring the dynamics of colliding elastic bodies has been a topic of research for many years. Many industrial applications require the prediction of such dynamical responses in their design process [1]. Through unilateral contact forces preventing inter-penetration of matter, a collision initiates a disturbance in the form of a stress wave. Analytical solutions are only known for simple cases such as longitudinal collision of simple rods or transverse contact of beams [2]. For more general configurations, the solution should be approximated numerically. However, common numerical methods, such as finite element methods combined with time-stepping schemes, exhibit limitations that might be unacceptable [3, 4]. Indeed, the obtained approximations may feature spurious oscillations (commonly known as Gibb’s phenomenon) and the associated wave propagation velocity may be different from its exact counterpart due to period lengthening and amplitude decreasing, resulting in *dispersion* and *dissipation* errors. Most energy-preserving numerical schemes dedicated to contact dynamics feature numerical dispersion issues [4].

In the framework of undamped linear continuous systems, natural modes of vibration are characterized by their natural frequencies (eigenvalues) and normalized shapes (eigenfunctions) [5]. In the phase space, linear modes can be seen as continuous families of periodic orbits describing planes. For nonlinear systems with smooth nonlinearities, the natural modes of vibration are regarded as extensions of their linear counterparts and are usually defined as two-dimensional manifolds in the phase space tangent to a linear mode at the equilibrium point [6]. These manifolds are invariant, *i.e.* for any initial condition on the manifold the solution will remain on it as time advances [7]. Additionally, nonlinear natural frequencies depend on the total energy of the system.

Most investigations and developments on nonlinear modal analysis have dealt with smooth nonlinearities [6], *i.e.* nonlinear terms differentiable with respect to the unknown of the problem, mostly polynomial functions of the displacement and velocity. The mechanical system investigated in this contribution involves unilateral contact conditions *stricto sensu*. As a consequence, neither displacements, neither velocities nor accelerations are differentiable in the usual sense with respect to time and space. These systems are known as *nonsmooth systems* [8] and the modes of these systems will be referred to as *nonsmooth modes* (NSM) in the following sections. Modes of vibration in nonsmooth systems have already been explored after a certain degree of regularization where the solution methods rely on the smoothness of the governing equations [9, 10, 11]. Likewise, they have been investigated in the framework of discrete systems [12, 13, 14].

Finding periodic solutions requires numerical methods which preserve total energy and are not prone to numerical dispersion. A considerable amount of research has been devoted to this topic with limited success [15, 16, 17]. In the present work, the Wave Finite Element Method (WFEM) initially developed in [18] is implemented in order to numerically approximate the modes of vibration of the one-dimensional finite elastic bar subject to frictionless unilateral contact constraints. Three different configurations are inspected: unstressed (positive gap at rest), prestressed (“negative” gap at rest) and initially grazing (zero gap at rest). The WFEM is a shock-capturing method—similar to the Godunov method [19] commonly used in computation fluid dynamics—which consists in finding and tracking waves propagating in a mechanical system. Such shock waves are expected in this work because of the presence of the unilateral contact condition. The proposed method does neither introduce artificial dissipation of energy nor numerical dispersion and it has successfully been used for the simulation of shock wave propagation in elastic solids, yet in the restricted context of one-dimensional domains [20, 18]. Multidimensional problems incorporating contact conditions are not targeted in this work due to the expected intricate interaction of compressional and shear waves with the boundaries and the possibility of a complicated contact interface.

The paper is organized as follows. The considered one-dimensional system is detailed in section 2. The capability of the WFEM to solve contact dynamics problems is illustrated, in section 3, using a benchmark problem with a known exact solution. The chosen approach for the search of periodic solutions is described in section 4. A method to numerically approximate the nonsmooth modes of the investigated system is presented in section 5. The approximate nonsmooth modes are then analyzed and characterized in section 6 (no formal proofs are given).

Lastly, nonsmooth modes of the considered system are compared to its forced response in section 7. Details about WFEM and its implementation are thoroughly described in Appendix A for a one-dimensional problem. The enforcement of contact constraints within the WFEM is detailed in Appendix B.

2. System of interest

The system of interest is a homogeneous elastic bar of length L and constant cross-sectional area S rigidly fixed to the ground at its left end and whose right end is subject to a conservative unilateral constraint as shown in Fig. 1. Its initial deformation at time $t_0 = 0$ is $\varepsilon_0(x)$ and its initial velocity is $v_0(x)$ where

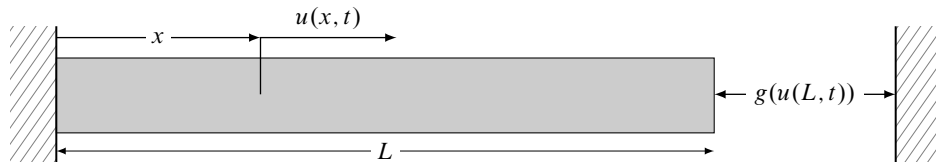


Figure 1: 1-D finite elastic bar subject to unilateral contact constraints

$x \in [0; L]$ is the coordinate of a point of the bar along its longitudinal axis in the initial configuration. Its mass per unit volume is denoted by $\rho > 0$ and $E > 0$ stands for Young’s modulus which are both, by assumption, space and time independent. Any elastic wave traveling within the bar thus propagates at constant velocity $c = \sqrt{E/\rho}$. The signed distance between the right end of the bar and the obstacle, or *gap function*, is defined as $g(u(L,t)) = g_0 - u(L,t)$, where g_0 is the signed distance between the unconstrained resting position and the obstacle. The unknown displacement, velocity and stress fields are denoted by $u(x,t)$, $v(x,t)$, and $\sigma(x,t)$ respectively; the quantity $r(t)$ is the unilateral contact force emerging at $x = L$ during gap closure. In linear elasticity, the stresses read $\sigma = E\varepsilon$ where the axial strains $\varepsilon = u_{,x}$ should be physically admissible, that is $u_{,x} > -1$. Stresses are related to the contact force r by

$\sigma(L, t) = Eu_{,x}(L, t) = r(t)/S$. There is no other external force acting on the system, either per unit length or pointwise at the boundary. The full formulation reads:

- Local equation:

$$\rho u_{,tt} - Eu_{,xx} = 0, \quad \forall x \in]0; L[, \quad \forall t > 0 \quad (1)$$

where $(\bullet)_{,tt}$ denotes the second derivative in time and $(\bullet)_{,xx}$, the second derivative in space.

- Boundary condition at $x = 0$:

$$u(0, t) = 0, \quad \forall t > 0 \quad (2)$$

- Complementarity conditions at $x = L$:

$$g(u(L, t)) \geq 0, \quad r(t) \geq 0, \quad r(t)g(u(L, t)) = 0, \quad \forall t > 0 \quad (3)$$

- Initial conditions:

$$u(x, 0) = u_0(x), \quad v(x, 0) = v_0(x), \quad \forall x \in]0; L[\quad (4)$$

This problem has a unique solution which conserves the total energy [21]. The local equation is also known as the *wave equation* defined on a finite domain and the exact solution to this problem, known in the literature as *D'Alembert's solution*, can be written as a sum of backward and forward travelling waves propagating with velocity c [2]. For given initial conditions $u(x, 0) = u_0(x)$ and $v(x, 0) = v_0(x)$, the displacement reads:

$$u(x, t) = \frac{1}{2} [u_0^*(x + ct) + u_0^*(x - ct)] + \frac{1}{2c} \int_{x-ct}^{x+ct} v_0^*(s) ds, \quad \forall x \in [0; L], \quad \forall t > 0 \quad (5)$$

where, depending on the considered boundary conditions (BC), u_0^* and v_0^* are periodic extensions on the real axis of u_0 and v_0 , defined on $[0; L]$ only.

Non-trivial periodic solutions of the contact problem described by Eqs. (1) to (4) are successions of free phases (open gap) and contact phases (closed gap). They can therefore be understood as the combination of solutions to an hyperbolic Partial Differential Equation with a switching boundary condition at $x = L$ between vanishing stress when the gap is open to prescribed displacement when the gap is closed. The nonlinearity in the formulation comes from the fact that the switching time is not known in advance. There is also a subtlety due to the change of length of the resting bar from one BC to another: while the fixed-free bar has a length L at rest, the latter becomes $L + g_0$ for the fixed-fixed bar. Then

- odd and even periodic extensions of period $4L$ are used for the free-fixed case:

$$\phi(y) = \begin{cases} -\phi(2L + y) & -2L < y < -L \\ -\phi(-y) & -L < y < 0 \\ \phi(y) & 0 < y < L \\ \phi(2L - y) & L < y < 2L \end{cases} \quad \text{and} \quad \phi(y + 4L) = \phi(y) \quad (6)$$

- odd periodic extensions of period $2L$ are used for the fixed-fixed case:

$$\phi(y) = \begin{cases} \phi(y) & 0 < y < L \\ -\phi(-y) & -L < y < 0 \end{cases} \quad \text{and} \quad \phi(y + 2L) = \phi(y) \quad (7)$$

where ϕ is a generic function displaying the properties to be satisfied by u_0^* and v_0^* [22]. The question is now to find the two functions u_0^* and v_0^* generating a state of the system which satisfies the local equation (1) and properly switches between fixed-free and fixed-fixed BC to comply with the unilateral contact conditions (3). This is achieved using the Wave Finite Element Method.

3. Illustration of the capabilities of WFEM

The WFEM is completely described, including a readily-implementable algorithm, in Appendix A (the WFEM method) and Appendix B (treatment of unilateral contact conditions in WFEM). In short, the unknown stresses and velocities are stacked into a state vector \mathbf{q} . Then, the system is discretized simultaneously in space and time with mesh sizes $\Delta x = L/N$ and $\Delta t = \Delta x/c$ respectively, where N is the number of cells used for discretization in space. The overall dynamics is approximated by $\mathbf{Q}^{(n)} = \mathbf{A}\mathbf{Q}^{(n-1)}$ where $\mathbf{Q}^{(n)} = [\mathbf{Q}_1^{(n)} \dots \mathbf{Q}_N^{(n)}]$ and $\mathbf{Q}_i^{(n)}$ is the average of state \mathbf{q} over cell C_i for $i = 1, \dots, N$ at time $t_n = n\Delta t$. The matrix \mathbf{A} encompasses stiffness and inertial terms as well as the boundary conditions (fixed-fixed or fixed-free here).

In this section, the capabilities of the WFEM are succinctly illustrated on a unilaterally constrained one-dimensional bar benchmark [3]. It can be compared to other time-integration schemes based on a semi-discretization in space through the Finite Element Method [20]. The problem consists of a homogeneous elastic rod of length L and constant cross-sectional area S and bouncing against an obstacle as shown in Fig. 2. Parameters reported in [3] are considered and listed in Tab. 1. A periodic solution is expected for well

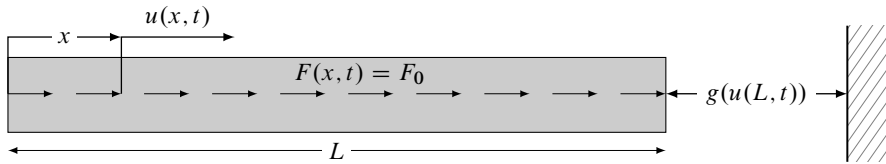


Figure 2: Benchmark bouncing homogeneous elastic bar (used in section 3).

chosen initial conditions. The displacement, velocity, contact force and total energy of the periodic motion of the contacting end are displayed in Fig. 3. These results were obtained using $N = 100$ cells and it matches the exact solution with a maximum relative error of $10^{-6} \%$.

Table 1: Simulation parameters for the considered benchmark, from [3]

Parameter	Value
Young's Modulus, E	900 Pa
Density, ρ	1 kg m ⁻²
Rod Length, L	10 m
Initial Gap, g_0	5 m
External Body Force, F_0	10 N m ⁻¹
Wave Velocity, $c = \sqrt{E/\rho}$	30 m s ⁻¹

As opposed to the FEM exhibiting Gibb's phenomenon or energy dissipation [3], the WFEM is capable of retrieving accurately the solution with a reasonable number of cells. Moreover, conventional FEM requires the use of an impact law leading to unavoidable drawbacks, such as the incompatibility between a contact phase of finite duration and energy conservation [4]. None of these issues are present with the WFEM approach. This is partly due to the fact that shock wave propagation is accurately captured in WFEM for our example.

As stated in [23], traditional numerical schemes commonly based on the standard Finite Element Method and dedicated to contact dynamics show spurious oscillations on the contact displacement and stress. Moreover, these oscillations do not disappear when the time step decreases and might increase instead. Various solutions have been proposed to alleviate these difficulties, mainly by adapting the time-domain discretization. They all fail by either adding non-physical damping, or not strictly respecting the contact constraint. This is partly explained by the inability of standard finite elements to properly propagate information.

4. Periodic solutions

Nonsmooth modes (NSM) are regarded as continuous families of periodic solutions satisfying the unilateral contact conditions. Accordingly, this research targets periodic solutions to problem Eqs. (1) to (4). Finding a periodic solution translates to finding initial conditions $u_0(x)$ and $v_0(x)$ and a period T which generate a

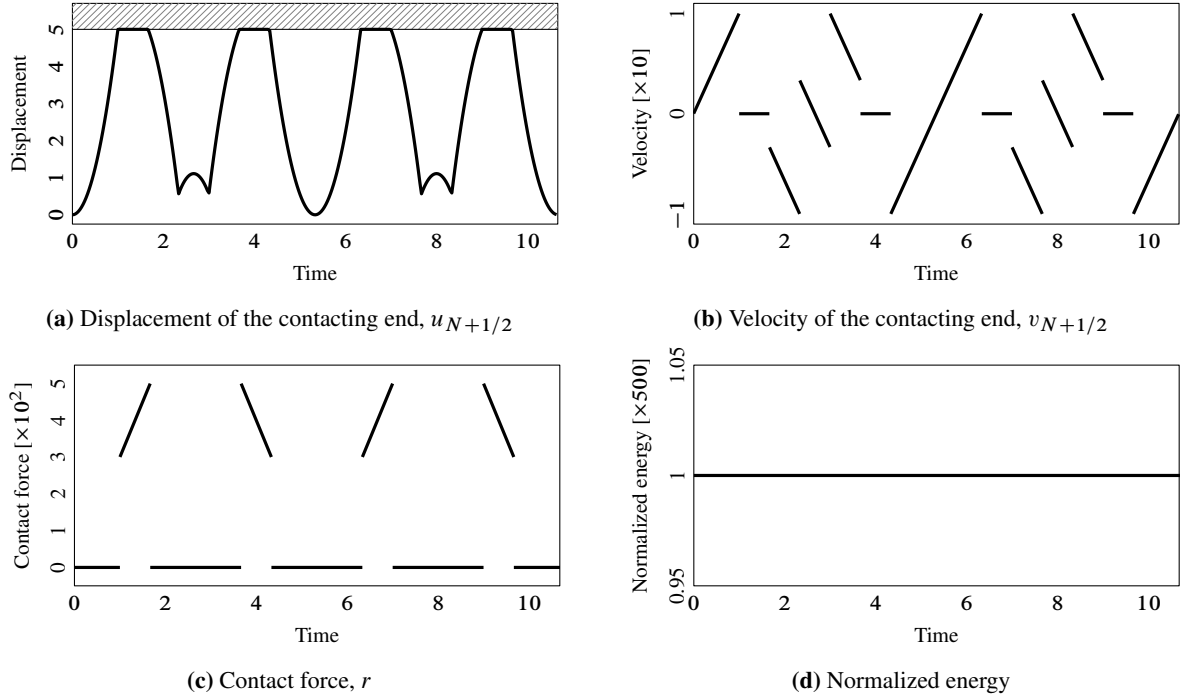


Figure 3: Periodic motion of the bouncing bar obtained by WFEM.

solution satisfying Eqs. (1) to (4) and the periodicity conditions

$$\begin{cases} u(x, t + T) = u(x, t) \\ v(x, t + T) = v(x, t) \end{cases}, \quad \forall x \in [0; L], \quad \forall t > 0. \quad (8)$$

Without loss of generality, it is assumed that a period starts with a free phase at $t = 0$ and ends with a contact phase at $t = T$. In the general case, a pattern of free and contact phases will arise within one period. The k successive transition instants between free and contact phases are denoted by T_i with $0 < T_1 < \dots < T_{k-1} < T_k$ and $T_k = T$ and are unknown. The sought solution is then a combination to be found of functions of the form (5) where u_0^* and v_0^* alternate between form (6) over $[0; T_1]$, $[T_2; T_3]$, etc. and form (7) over $[T_1; T_2]$, $[T_3; T_4]$, etc., such combination being finally periodic in time. Combining these portions of D’Alembert solutions in order to form a periodic solution is a formidable task.

The WFEM approximately solves the above problem by building two matrices, \mathbf{A}_f for the free–fixed BC and \mathbf{A}_c for the fixed–fixed BC, so that mapping an initial state to the current state after a succession of free and contact phases is straightforward via Eq. (A.22). In contrast to more commonly-used time-integration schemes based on FEM, the WFEM perfectly preserves energy (in this one-dimensional configuration at least), which is crucial for the computation of periodic solutions. Additionally, this scheme, for the problem at hand at least, is not prone to numerical dispersion and does not suffer from the well-known Gibb’s phenomenon commonly observed in unilateral contact dynamics [3].

The FEM framework without regularization of the complementarity conditions in continuous time is used for the calculation of nonsmooth modes in [13, 24, 14]. However, the formulation relies on a space-discretization and hence requires the incorporation of an impact law—for instance Newton’s impact law—to ensure the well-posedness of the problem. Since energy conservation is necessary to find nonsmooth modes, a perfectly elastic impact law should be considered, from which would emanate impulsive dynamics. This excludes periodic motions with “lasting” non-impulsive contact phases similar to those of the periodically bouncing elastic bar exposed earlier. By simultaneously discretizing the governing equations in space and time in accordance with the characteristic lines, the WFEM accurately propagates shock waves: this is probably why no impact law is needed in this framework.

5. Nonsmooth modal analysis

Nonsmooth modal analysis consists in the characterization of the vibratory properties of autonomous mechanical systems with nonsmooth nonlinearities [12, 13, 24] such as those induced by as unilateral contact conditions. This is achieved by finding one-parameter continuous families of periodic trajectories forming

manifolds in the phase space. In this work, the targeted solutions are assumed to comprise *free phases* (open gap) as well as *contact phases* (closed gap), as described in section 4. An example of an admissible periodic displacement with two free phases and two contact phases is depicted in Fig. 4.

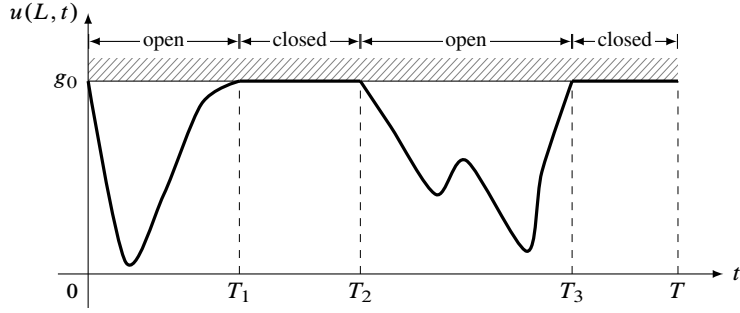


Figure 4: Admissible periodic displacement of the contacting bar end with closed and open gap switches.

5.1. Problem formulation

As seen in Eq. (A.28), the motion of the system is uniquely determined by the initial conditions, as in any deterministic system. The aim is to find such initial conditions which generate a periodic motion in the spirit of shooting methods [25]. If such periodic solutions exist, the formulation reduces to finding their period T and the appropriate initial conditions satisfying

$$\mathbf{q}(x, T) = \mathbf{q}(x, 0), \quad \forall x \in [0; L]. \quad (9)$$

In the discrete setting of the WFEM, this translates to finding n_T and the initial conditions $\mathbf{Q}^{(0)}$ such that

$$\mathbf{Q}^{(n_T)} = \mathbf{Q}^{(0)} \quad (10)$$

where n_T is the number of steps required to cover the period T . In the simplest case, the sought periodic solutions are only composed of one fixed–free phase and one fixed–fixed phase per period¹ even though more complicated patterns are expected to exist. Then, the solution is assumed to be composed by m consecutive steps in open contact (free phase) and p consecutive steps in closed contact (contact phase).

Invoking Eq. (A.22), the state of the system after $n_T = m + p$ time steps emanating from initial state $\mathbf{Q}^{(0)}$ reads

$$\mathbf{Q}^{(n_T)} = \mathbf{A}_c^p \mathbf{A}_f^m \mathbf{Q}^{(0)}, \quad (11)$$

with the origin of time taken at the beginning of the free phase. Both matrices \mathbf{A}_c and \mathbf{A}_f are known, see Appendix A. The duration of free and contact phases corresponding to periodic motions are not known a priori, so the integers m and p leading to acceptable solutions are unknowns of the problem. By enforcing the periodicity conditions, Eq. (11) simplifies to

$$(\mathbf{A}_c^p \mathbf{A}_f^m - \mathbf{I})\mathbf{Q}^{(0)} = \mathbf{0}. \quad (12)$$

An initial condition $\mathbf{Q}^{(0)}$ satisfying Eq. (12) is called a “potential solution” for given p and m . Indeed, potential solutions may not be actual solutions of the initial problem: nothing prevents them from penetrating the rigid foundation during free phase and/or the corresponding contact force could be non-negative: these conditions cannot be enforced in Eq. (12). Consequently, potential solutions are called *admissible* solutions if they satisfy the following additional conditions:

COND1 Free phase: $u_{N+1/2}^{(n)} \leq g_0$ and $r^{(n)} = 0$ for $n = 0, 1, \dots, m$.

COND2 Contact phase: $u_{N+1/2}^{(n)} = g_0$ and $r^{(n)} \leq 0$ for $n = m + 1, m + 2, \dots, m + p$.

COND3 Material impenetrability: $\varepsilon_i^{(n)} > -1$ for $n = 0, 1, \dots, m + p$ and $i = 1, \dots, N$.

where $u_{N+1/2}^{(n)} \approx u(L, T)$ and $\varepsilon_i^{(n)}$ is the discretized strain field. To summarize, periodic solutions satisfying contact conditions are obtained by solving the problem: Find $m \in \mathbb{N}^*$, $p \in \mathbb{N}^*$, and initial condition $\mathbf{Q}^{(0)} \in \mathbb{R}^{2N}$ such that Eq. (12) together with **COND1**, **COND2** and **COND3** are simultaneously satisfied.

¹With this assumption, the solution features one gap closure and one gap opening per period.

5.2. Solution procedure

For specified m and p , a periodic motion necessarily corresponds to an initial condition which is in the kernel of the operator $\mathbf{S}_T = \mathbf{A}_c^p \mathbf{A}_f^m - \mathbf{I}$ as highlighted in Eq. (12), that is $\mathbf{Q}^{(0)} \in \ker \mathbf{S}_T$. The dimension h of $\ker \mathbf{S}_T$ depends on the doublet (m, p) . A non-trivial solution may exist only if $h > 0$. If $h > 0$ and $\{\mathbf{e}_1, \mathbf{e}_2, \dots, \mathbf{e}_h\}$ is a basis of $\ker \mathbf{S}_T$, then $\mathbf{Q}^{(0)} = \alpha_1 \mathbf{e}_1 + \alpha_2 \mathbf{e}_2 + \dots + \alpha_h \mathbf{e}_h$ for some $\alpha_1, \alpha_2, \dots, \alpha_h$. The state $\mathbf{Q}^{(n)}$ is completely determined by $\mathbf{Q}^{(0)}$ via Eq. (A.28). Accordingly, $\mathbf{Q}^{(n)}$ can be expressed in terms of the coefficients $\alpha_1, \alpha_2, \dots, \alpha_h$ only and it suffices to find appropriate values such that **COND1**, **COND2** and **COND3** are satisfied.

Finding m, p such that $h > 0$ is achieved by systematically computing h for every combination of m and p within a given range. Once an admissible solution is known, other admissible solutions can be straightforwardly found in its vicinity. As soon as a continuum of periodic orbits—involving one contact phase and one free phase—emerges, it defines a nonsmooth mode of vibration.

6. Results and discussion

In this section, the approach described in section 5 is implemented to construct nonsmooth modes of vibration of the system described in section 2. The parameters E, ρ and L are arbitrarily chosen to be unity and units are discarded. The results are obtained for 1000 cells. The time step is calculated accordingly, i.e. $\Delta t = \Delta x/c = 1/1000$.

In the linear framework (that is without the contact conditions), *linear natural frequencies* of vibration denoted ω_k for free–fixed boundary conditions and Ω_k for fixed–fixed boundary conditions are

$$\omega_k = \frac{(2k-1)\pi c}{2L} = (2k-1)\omega_1 \quad \text{and} \quad \Omega_k = \frac{k\pi c}{L} = k\Omega_1, \quad k \in \mathbb{N}^*. \quad (13)$$

It is expected that the slightly damped linear system under consideration periodically forced in a neighborhood of these frequencies will resonate. Conversely, in the nonlinear framework (that is with contact conditions), such frequencies do not have the same physical interpretation anymore: the nonlinear system will resonate close to other unknown frequencies which are calculated by the nonsmooth modal analysis, for a given level of energy. The nonlinear system can also feature internal resonances where two or more NSM interact [26]; for instance, exciting the system in the neighborhood of a high-frequency NSM may generate a large amplitude low-frequency NSM [6]. Note that the system of interest satisfies a complete internal resonance condition in the sense that ω_k and $\Omega_k, k = 2, \dots, \infty$ are multiples of ω_1 and Ω_1 , respectively. Moreover, a nonlinear system may exhibit subharmonic and superharmonic resonances in the vicinity of $(p\omega_k)/q$, for p, q positive integers such that $0 < p/q < 1$ and $1 < p/q$, respectively [6].

In this contribution, Frequency–Energy plots are preferably used, quoting [6]: “a nonlinear modal motion is represented by a point in such plots, which are drawn at a frequency corresponding to the minimal period of the periodic motion and at an energy equal to the conserved total energy during the periodic motion. A branch, represented by a solid line, is a family of nonlinear modal motions possessing the same qualitative features.” The reported frequencies are normalized with respect to ω_1 and the energy is normalized with respect to the energy of the first linear mode grazing orbit satisfying

$$\max_{t \in \mathbb{R}} u(L, t) = g_0. \quad (14)$$

When the calculated periodic solutions have one free phase and one contact phase, *admissible* solutions are only found when $h = 1$ for various (m, p) . For $h \geq 2$, there exists an infinite set of *potential* solutions, but none satisfy **COND1** and **COND2**. After many numerical experiments, admissible solutions could be found only when h equals the number of contact phases.

Once a solution is found, a point in the NSM branch is defined by the total energy of the *admissible* periodic motion and the respective frequency $\omega = 2\pi/T$, see Fig. 5.

If the initial gap is positive $g_0 > 0$ (unstressed bar at rest), NSM branches arise in the vicinity of the linear natural frequencies ω_k and subharmonics $(p\omega_k)/q$, and present hardening behavior. For a “negative” gap $g_0 < 0$ (initially prestressed bar), the NSM branches start in the vicinity of linear natural frequencies Ω_k and present softening behavior. The frequency–energy dependence—i.e. hardening and softening behavior—exhibited by NSM is a typical feature of nonlinear systems [6]. Similar results were already obtained for simplified discrete models for the unstressed case with penalized contact constraints [9, 10] and with a non-smooth formulation [12].

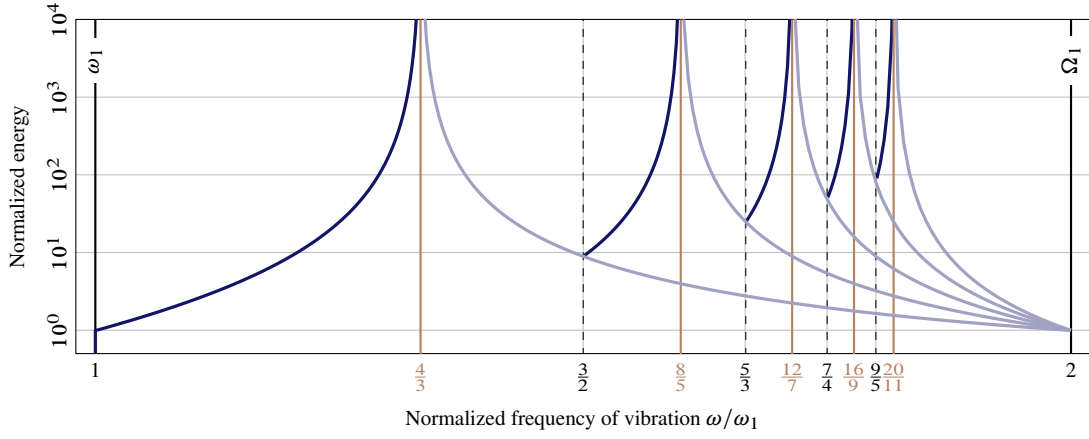


Figure 5: Frequency–Energy plot in the range $[\omega_1, \Omega_1]$ for $g_0 > 0$ [—], $g_0 = 0$ [—] and $g_0 < 0$ [—] with a few subharmonics of linear modes [—].

On the other hand, if the bar is initially grazing with the rigid foundation, that is $g_0 = 0$, then the NSM branches are the common vertical asymptotes to the previous backbone curves, as shown in Figs. 5 and 6 for the first and second NSM, respectively. Internal resonance branches, explored in subsection 6.3, have been omitted in these figures. Interestingly, when $g_0 = 0$ the system mimics a linear behavior where the frequency of the orbits does not depend on their energy.

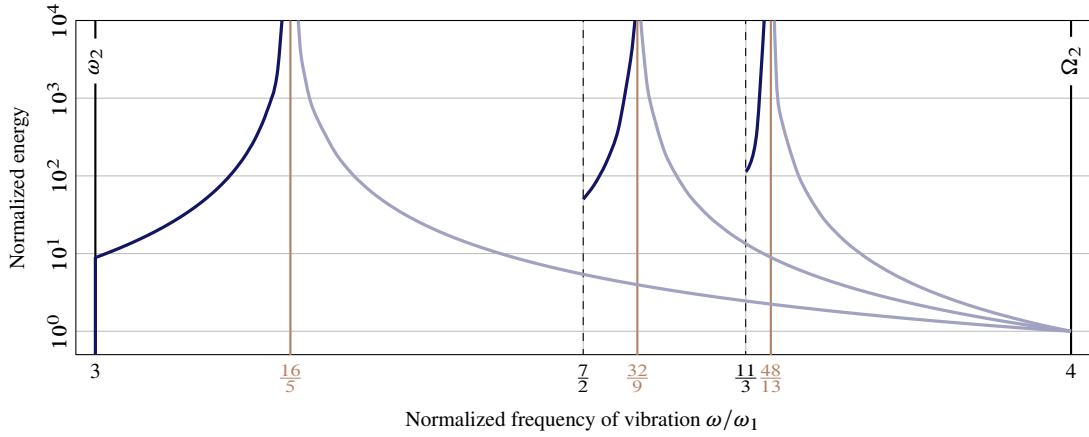


Figure 6: Frequency–Energy plot in the range $[\omega_2, \Omega_2]$

Though the behavior and ranges of frequencies of the NSM branches depend on the sign of g_0 , they “converge” to the branches of $g_0 = 0$ when $g_0 \rightarrow 0$, as seen in Fig. 7 for the main NSM branch in the range $[\omega_1, \Omega_1]$. In other words, there is no significant difference between NSM with very small positive initial

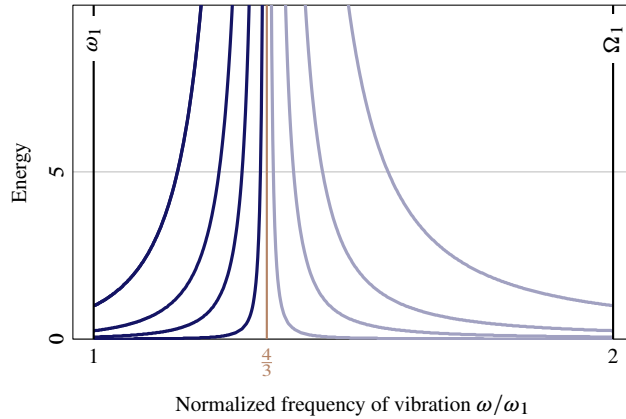


Figure 7: Sensitivity of the first NSM branch to g_0 . Energy is not normalized. The backbone curves for $g_0 \neq 0$ and $g_0 \rightarrow 0$ slowly “approach” the backbone curve for $g_0 = 0$.

gap, zero initial gap or very small initial negative gap. Moreover, the normalized shape of the backbone

curves depend only on the sign of g_0 . Without loss of generality and for illustration purposes, $g_0 = \pm 10^{-3}$ or $g_0 = 0$ in the remainder.

In the following sections, a detailed study of the NSM branches is presented. It should be noted that all the results were obtained numerically. The proposed results have to be read as conjectures.

6.1. Main backbone curves

The main backbone curves are defined as the NSM branches, in the Frequency–Energy plot, starting in the vicinity of:

- ω_k , the k -th linear natural frequency for free–fixed BC, for positive initial gap $g_0 > 0$,
- Ω_k , the k -th linear natural frequency for fixed–fixed BC, for negative initial gap $g_0 < 0$.
- For zero initial gap $g_0 = 0$, the main backbone curve is a vertical line asymptotic to its two above counterparts. Such asymptotes are located at $\omega_1(\omega_k/\omega_1 + 1)^2/(\omega_k/\omega_1 + 2)$.

Periodic motions corresponding to the main backbone curves in the range $[\omega_1, \Omega_1]$ are depicted in Fig. 8. A generic space-time plot of the displacement of the bar is provided in Fig. 8(a). The solution is the

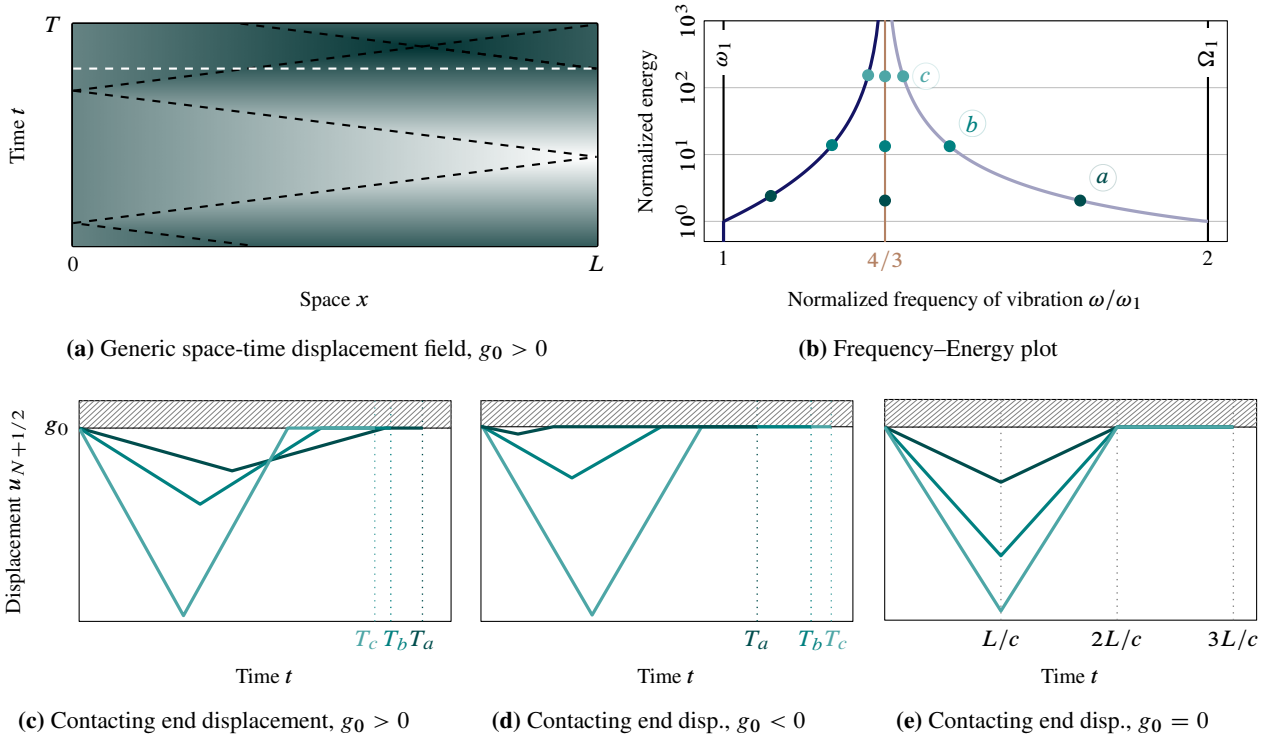
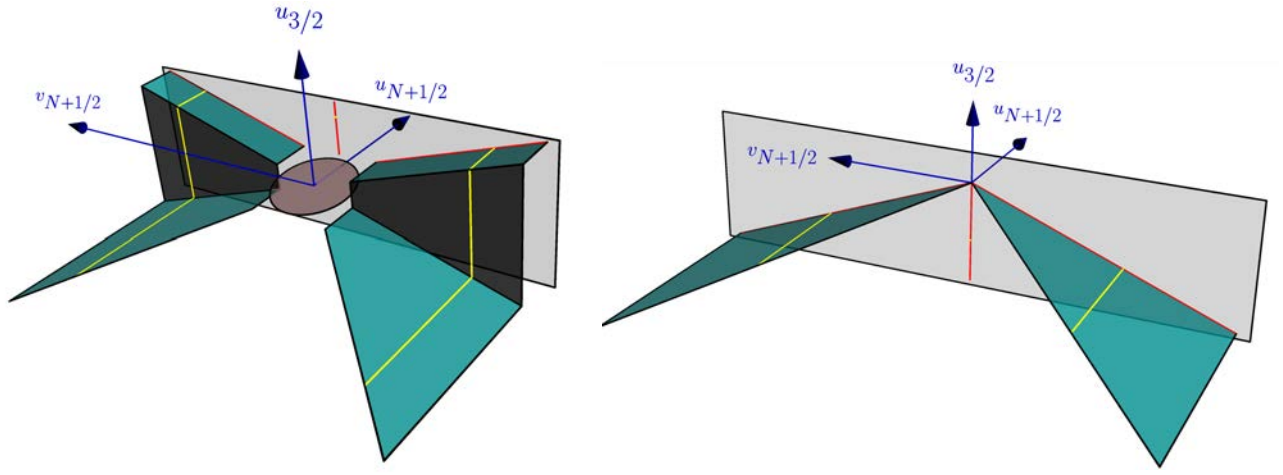


Figure 8: Periodic motions on the main backbone curve in the range $[\omega_1; \Omega_1]$ for one contact phase per period. Positive displacement corresponds to dark green and negative displacement, to white. Black dashed characteristic lines ($t = \pm x/c$). White dashed line indicates when contact closes.

combination of interacting forward and backward traveling waves which propagate along the characteristic lines ($t = \pm x/c$), as opposed to the linear counterpart modal motions which are standing waves [2]. The corresponding periodic displacements of the contacting end are shown in Figs. 8(c), 8(d), and 8(e) with corresponding backbone curve states in Fig. 8(b). All the periodic solutions living in the main backbone curve comprise one free phase and one contact phase. For a positive as well as negative initial gap, the time of contact phase is increasing and the time of free phase decreases as the frequency of vibration increases. When the initial gap is zero, NSM have constant period equal to $T = 3L/c$ and the duration of contact closure is L/c while the free phase time is $2L/c$. It should also be noted that the contact force associated to all the depicted motions is piecewise constant on a period.

The invariant manifolds are plotted in the cross-section $(u_{N+1/2}, v_{N+1/2}, u_{3/2})$ —*i.e.* (displacement of the contacting end of the bar, velocity of the contacting end of the bar, displacement of the right-hand side interface of cell \mathcal{C}_1)—of the state-space in Fig. 9. The invariant manifold for $g_0 = 0$ is identical to the manifold for $g_0 < 0$. All computed manifolds are unions of flat planes and present a discontinuity along the velocity direction, as expected. When $g_0 > 0$, the linear portion of the first mode corresponds to an elliptical disk in the chosen frame as shown in Fig. 9. The linear and nonlinear portions of the manifold are not continuously connected because of the internal resonance property.

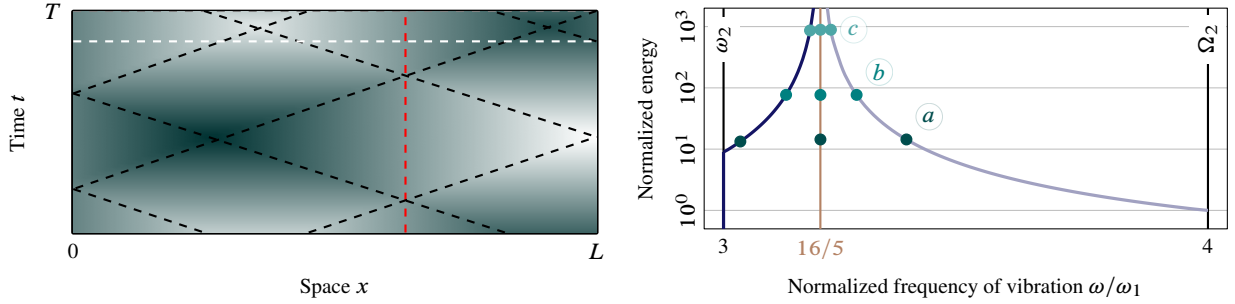


(a) Vicinity of ω_1 , $g_0 > 0$. Ellipse: linear portion of the manifold

(b) Vicinity of Ω_1 , $g_0 < 0$

Figure 9: Invariant manifold of the main backbone curve in the vicinity of ω_1 plotted in the cross-section $(u_{N+1/2}, v_{N+1/2}, u_{3/2})$. Gray surface: Poincaré cross-section $u_{N+1/2} = g_0$. Yellow line shows a periodic orbit. Red lines are intersections between NSM and the hyperplane.

The periodic motions corresponding to the main backbone curves in the range $[\omega_2, \Omega_2]$ are depicted in Fig. 10. The periodic displacements of the contacting interface have, as for the first NSM, one free phase and



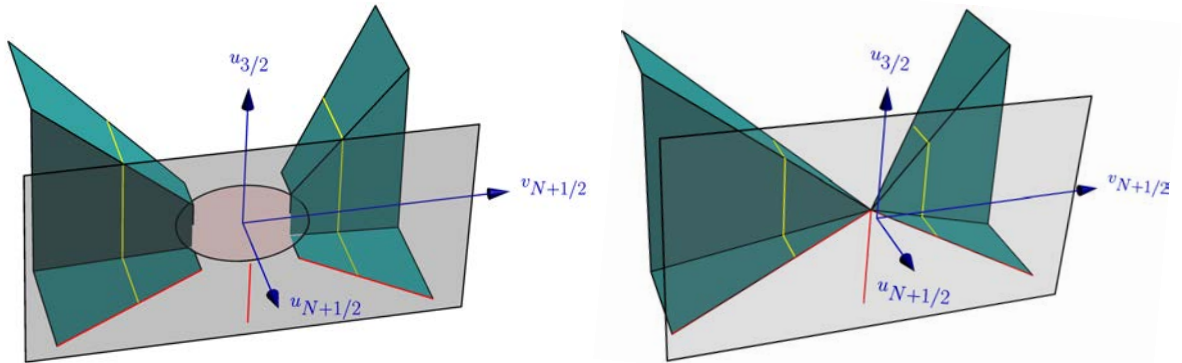
(a) Generic space-time displacement field, irrespective of g_0

(b) Frequency–Energy plot

Figure 10: Periodic motions corresponding to the main backbone curve in the range $[\omega_2; \Omega_2]$ with one contact phase per period. Positive displacement corresponds to dark green and negative displacement, to white. End bar displacements are similar to the ones reported in Figures 8(c), 8(d) and 8(e).

one contact phase, see Figs. 8(c), 8(d), and 8(e). Figure 10(a) depicts the generic space-time plot (irrespective of g_0), showing that the periodic solutions have one “node of vibration” along x —similar to the second linear mode of the clamped-free bar [2]. Furthermore, for $g_0 = 0$, the periodic displacements have a period of $5L/(4c)$ comprising one contact phase of duration $L/(4c)$ and one free phase of duration L/c .

The second NSM invariant manifolds are plotted in the cross-section $(u_{N+1/2}, v_{N+1/2}, u_{3/2})$, see Fig. 11. Similar to the first NSM, these projections present discontinuity in velocity due to the unilateral



(a) Vicinity of ω_2 , $g_0 > 0$. Ellipse: linear portion of the manifold

(b) Vicinity of Ω_2 , $g_0 < 0$

Figure 11: Invariant manifold of the second main backbone curve in the cross-section $(u_{N+1/2}, v_{N+1/2}, u_{3/2})$.

contact constraints and are unions of flat portions. For illustration purposes, only the first two NSM are

shown in this section. However, the presented approach can be also used to find higher frequency NSM which requires a smaller time-step Δt and therefore, greater computational time. By construction, the periodic solutions corresponding to the main backbone curves for higher NSM display a similar structure: one free phase and one contact phase. All computed NSM feature an increasing number of nodes of vibration along space for higher frequencies. For instance, the third NSM has two nodes of vibration.

6.2. Subharmonic backbone curves

For $g_0 > 0$, a *subharmonic backbone curve* emanates in the vicinity of a free–fixed BC linear subharmonic resonance frequency:

$$\frac{\omega_k(n+1) + n\omega_1}{n+1} = \frac{2k(n+1) - 1}{n+1}\omega_1, \quad n, k \in \mathbb{N}^*. \quad (15)$$

For $g_0 < 0$, a subharmonic backbone curve starts in the vicinity of Ω_k and shares an asymptote with the subharmonic backbone curve for positive initial gap. Furthermore, for $g_0 = 0$, a subharmonic backbone curve is asymptotic to the above counterparts. Several numerical experiments suggest that the asymptotes are located at

$$\frac{\omega_1(n+1)(\omega_k/\omega_1 + 1)^2}{\omega_k/\omega_1(n+1) + n + 2}, \quad n, k \in \mathbb{N}^*. \quad (16)$$

The number of computable subharmonics is determined by the discretization time-step; for example, Fig. 12 displays only six branches while the time step was $\Delta t = 10^{-3}$. The displacements of the contacting end of

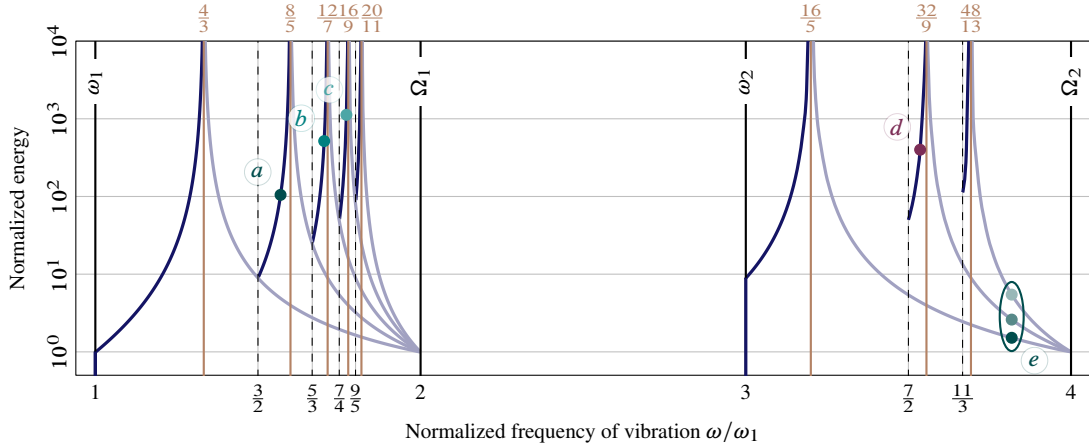


Figure 12: Main and subharmonic NSM branches within $[\omega_1, \Omega_2]$.

the bar of four periodic solutions, for $g_0 > 0$, lying in subharmonic backbone curves are depicted in Fig. 13. Their locations in the Frequency–Energy plot are indicated in Fig. 12. Figure 13 suggests that the periodic motions present n grazing instants and $k - 1$ nodes of vibration along x , when the NSM branch starts in the vicinity of the n -th subharmonic of ω_k , as inferred from Eq. (15). Interestingly, the periodic motions of the contacting end for points “a” and “d” are similar, however the latter has more nodes of vibration, as expected. Higher frequency content is also expected in periodic motions around subharmonics of higher NSM.

Figure 14 shows the invariant manifold corresponding to a subharmonic vibration in the vicinity of $\omega_2/2 = 3\omega_1/2$, noting from Eq. (13) that $\omega_2 = 3\omega_1$. This invariant manifold resembles the manifold of the second main NSM branch, depicted in Fig. 11, but with additional planes, corresponding to the free phase portion after the grazing instant, shown in red and overlapping with a portion of the green surface in Fig. 14. The periodic solutions living in this manifold jump from one surface to the other at contact times and at grazing times.

Additionally, when $g_0 < 0$, periodic solutions belonging to distinct NSM branches coexist when $g_0 < 0$, see “e” in Fig. 12. The corresponding periodic displacements of the contacting end are plotted in Fig. 15 where the period of vibration is the same. Here, the solutions have longer free phases and increasing number of grazing instants with higher energy. The grazing instants coincide with the switching BC time of lower energy solutions. The number of nodes is larger for high energy solutions, as already detailed above.

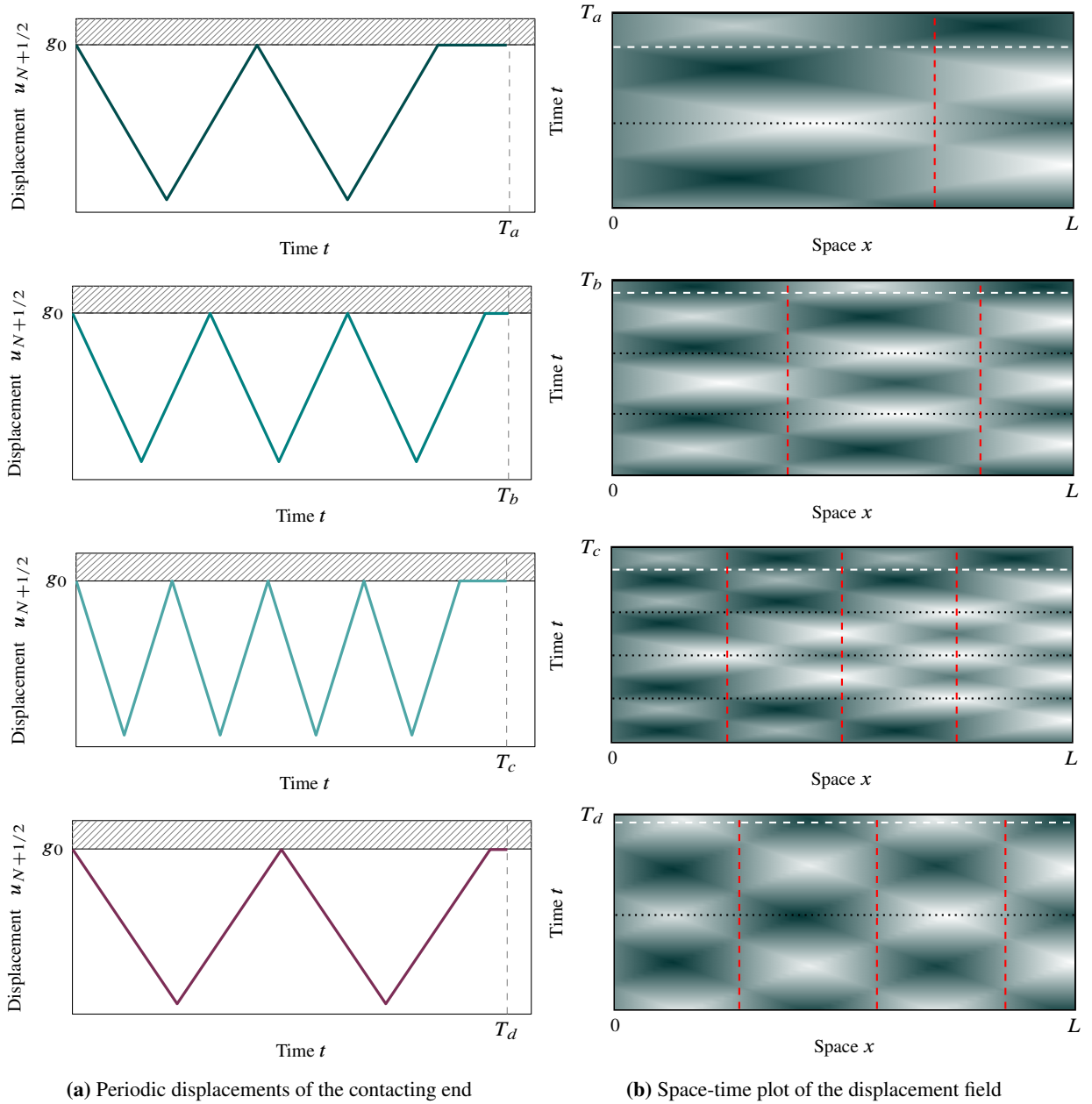


Figure 13: Periodic motions in the vicinity of $\omega_2/2 = 3\omega_1/2$ (top), $\omega_3/3 = 5\omega_1/3$ (top-center), $\omega_4/4 = 7\omega_1/4$ (bottom-center) and $\omega_4/2 = 7\omega_1/2$ (bottom) corresponding respectively to points “a”, “b”, “c” and “d” in Fig. 12. Positive displacement corresponds to dark green and negative displacement, to white. Black dotted lines correspond to the grazing instants.

Interestingly, extensive numerical experiments show that NSM branches do not appear in the range of frequencies $[\Omega_k, \omega_{k+1}]$, $k = 1, 2, 3, \dots$ as observed in Fig. 12. This could be due to the fact that linear modes of the fixed–fixed case embed higher energy in these frequency interval causing chaotic or quasiperiodic motions.

6.3. Internal resonance branches

By the nature of the employed numerical algorithm, WFEM cannot yield an actual continuum of solutions (see section 5). However, the periodic solutions previously presented are all part of an apparent continua. The proposed approach also leads to sparse periodic solutions, see clouds of points in Fig. 16. Presumably, these points are also part of continua stemming from main and subharmonic backbone curves, however much more challenging to capture numerically because of the high-frequency content in the corresponding mode shapes, see Fig. 17. These points seem to be organized in internal resonances backbone curves [6], which are ignored in the preceding sections. The data points depicted in Fig. 16 correspond to admissible periodic motions. They are organized on backbone branches emanating from the main one in the vicinity of the frequencies

$$\frac{2k}{2k-1}\omega_1, \quad k = 2, 3, \dots \quad (17)$$

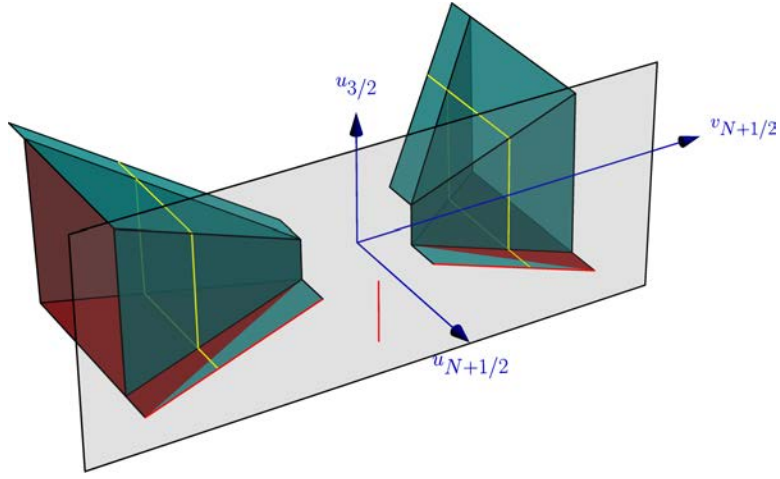


Figure 14: Invariant manifold in the vicinity of $\omega_2/2$ for $g_0 > 0$ in cross-section $(u_{N+1/2}, v_{N+1/2}, u_{3/2})$. Red planes generated after grazing instant.

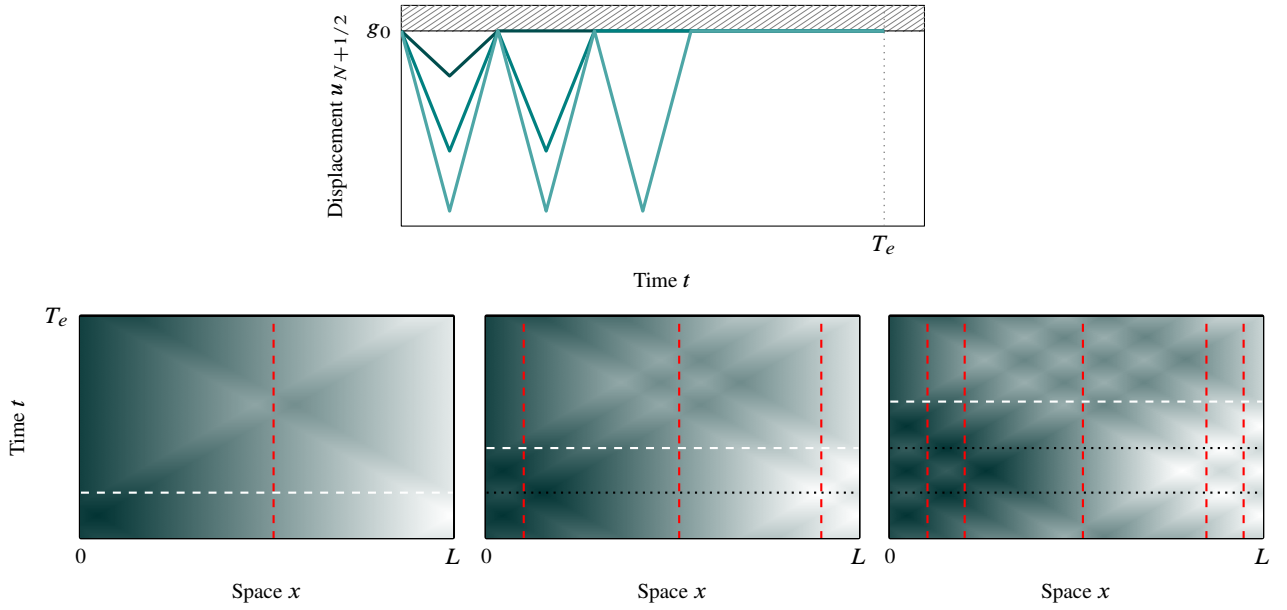


Figure 15: Periodic motions of the contacting end for coexisting solutions corresponding to points “e” in Fig. 12. Zero displacement corresponds to dark green and negative displacement, to white.

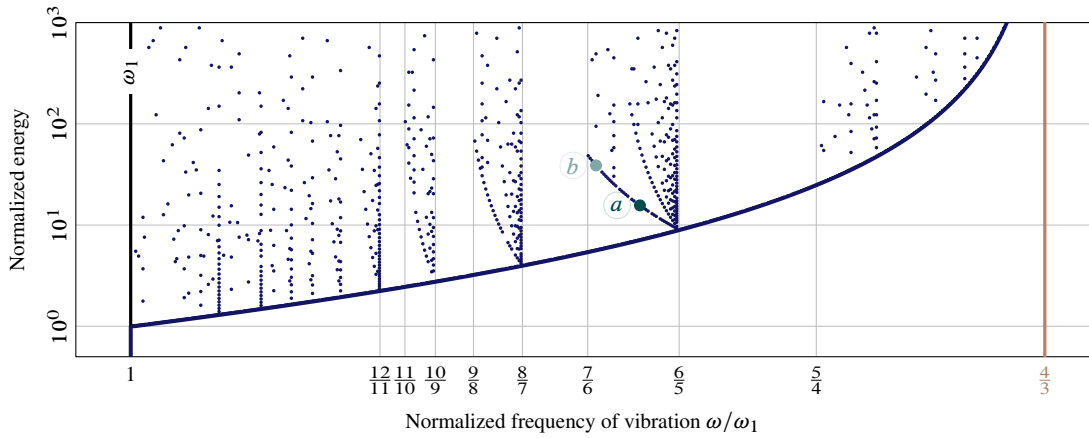


Figure 16: Main NSM branch around ω_1 with additional internal resonance branches.

Moreover, it is observed in Fig. 16 that there are no internal resonance branches in the frequency range $[(2k - 1)\omega_1/(2k - 2); 2k\omega_1/(2k - 1)]$, $k = 3, 4, \dots$, presumably because the solutions are quasiperiodic or chaotic in this range. Also, for a given frequency, multiple solutions might coexist, mimicking the behavior of the NSM branches of the initially grazing bar. This is not further explored in this work.

Periodic solutions featuring an internal resonance in the vicinity of $(\omega_3 + \omega_1)/5 = 6\omega_1/5$ are displayed in Fig. 17. These periodic motions present two grazing instants and appear to correspond to a modal interaction between the first NSM and the first subharmonic of the third NSM, as observed from Figs. 8(c) and 13. The corresponding intricate interaction of traveling waves is depicted in the space-time plot of the

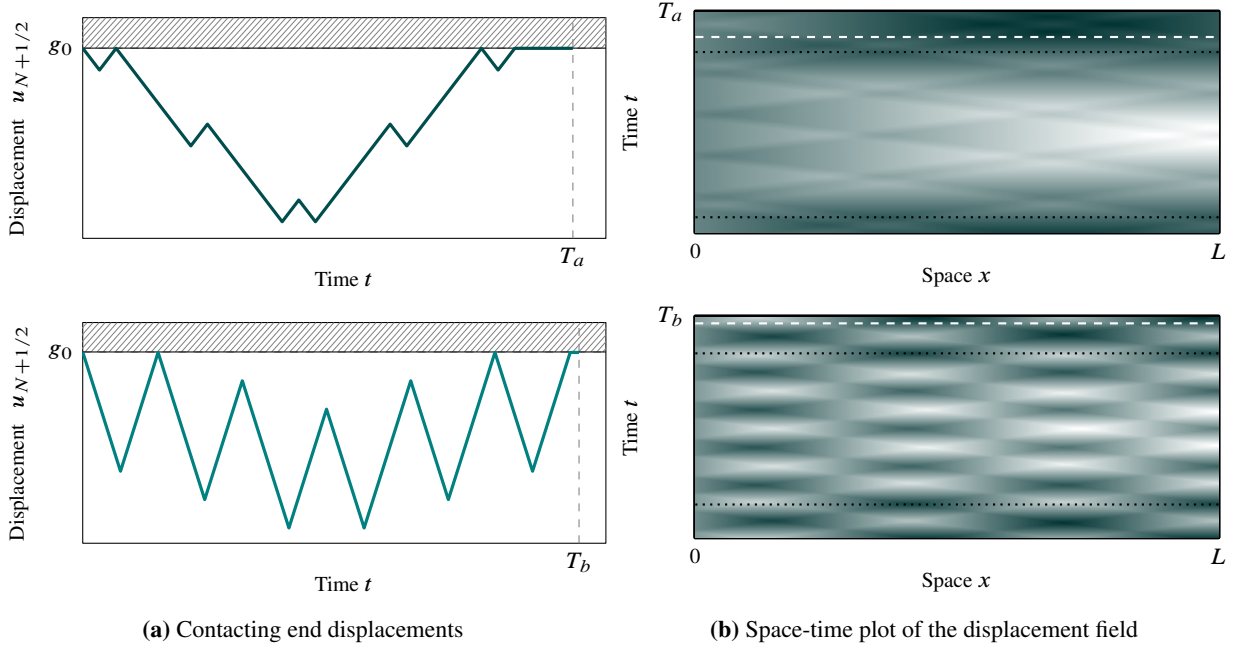


Figure 17: Internal resonances for $g_0 > 0$ in the vicinity of $(\omega_3 + \omega_1)/5 = 6\omega_1/5$: points “a” (top) and “b” (bottom) in Fig. 16. Positive displacement corresponds to dark green and negative displacement, to white.

displacement field in Fig. 17(b). Contrary to solutions of the main and subharmonic backbone curves for $g_0 > 0$, the contact duration of internally resonant periodic motions decreases with increasing frequency: they exhibit a softening behavior. Being a combination of low and high frequency modes, they present nodes of vibration along space as well as grazing instants, which are distinctive features of subharmonics and higher NSM.

It is difficult to compute the occurrence of internal resonances in systems involving unilateral contact. However, the data obtained by WFEM give suggestions about the existence of these NSM branches. The characterization of the periodic motions associated to internal resonances is helpful to predict the possible sudden resonance of real life applications, when vibrating around frequencies defined in Eq. (17).

6.4. Periodic solutions with two contact phases per period

The previous sections were devoted to solutions with one contact phase and one free phase per period, as expressed in Eq. (11). In this section, solutions with more than one contact phase per period are explored. The methodology is exactly the same, but there are two additional unknowns (duration of second contact phase $\ell \Delta t$ and duration of second free phase $m \Delta t$, ℓ and $m \in \mathbb{N}^*$) in the new equation

$$(\mathbf{A}_c^p \mathbf{A}_f^k \mathbf{A}_c^\ell \mathbf{A}_f^m - \mathbf{I}) \mathbf{Q}^{(0)} = \mathbf{0}, \quad (18)$$

to be compared with Eq. (12). It appears that non trivial solutions $\mathbf{Q}^{(0)}$ can be found only if the contact phases have same duration, that is $p = \ell$. This might be the consequence of the symmetry with respect to time and space of the wave equation.

For the matrix $\mathbf{S}_T = \mathbf{A}_c^p \mathbf{A}_f^k \mathbf{A}_c^p \mathbf{A}_f^m - \mathbf{I}$, families of periodic solutions satisfying contact conditions were found only when $h = \dim(\ker \mathbf{S}_T) = 2$ and $\dim(\ker \mathbf{S}_T)$ should equal the number of contact phases.

The solution procedure explained in subsection 5.2 leads to a one-dimensional continuum of periodic orbits emerging in the vicinity of $\omega_2/5 = 3\omega_1/5$, where $\omega_2 = 3\omega_1$, defining a subharmonic backbone curve with two contact phases. The corresponding NSM branch and the periodic displacement of the contacting end are depicted in Fig. 18, for $g_0 > 0$. Interestingly, it resembles the two impact-per-period trajectories of a serial spring–mass system constrained by an obstacle with a purely elastic contact law [14]. In particular, the solutions have two axes of symmetry per period along the time axis, which are located in the middle of each free phase.

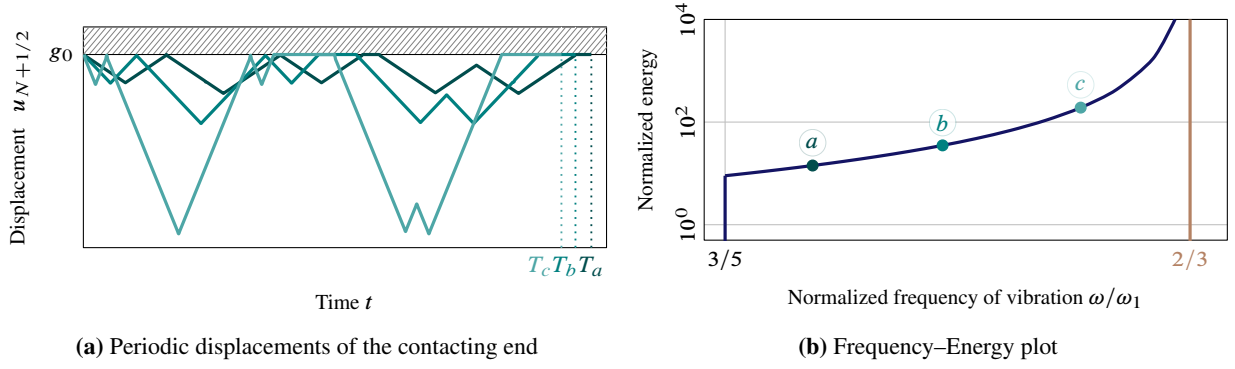


Figure 18: NSM branch in the vicinity of $\omega_2/5 = 3\omega_1/5$ for $g_0 > 0$.

The asymptote of this NSM branch appears to be located at $2\omega_1/3$. The displacements of the contacting end, shown in Fig. 18(a), have one free phase with two grazing instants. As in the case with one contact phase per period, the amplitude of the displacements and the duration of the contact phases gets larger with the frequency of vibration. A finer discretization is required to obtain additional NSM branches with higher number of contact phases. Presumably, these branches are highly important for the prediction of vibratory responses, where the elastic bar could resonate even if it is excited at a frequency lower than the first linear natural frequency ω_1 .

7. Forced response of a mechanical system subject to contact constraints

One important purpose of performing nonsmooth modal analysis of a mechanical system is to predict its behavior when periodically forced [24, 10]. Accordingly, the frequency response of the previously-investigated elastic bar with small damping and periodic external excitation is now compared to the NSM. The excitation consists in an external distributed harmonic force and/or a harmonically moving rigid wall that compresses the bar, see Fig 19. The force acting on the bar is $f(x, t) = f_0(x) \sin(\omega t)$ and the displacement of the moving wall is $w(t) = w_0 \sin(\omega t)$ where ω is the frequency of excitation and $w_0 > g_0$. The gap function is now defined as $g(u(L, t), w(t)) = g_0 + w(t) - u(L, t)$. The system has been slightly damped by adding a velocity-dependent term with a small viscous damping coefficient in the left-hand side of Eq. (1). The forced response of this system is obtained for various amounts of damping and was computed using the a WFEM version detailed in Algorithm 2 using a time-stepping approach not specifically targeting periodic motions.

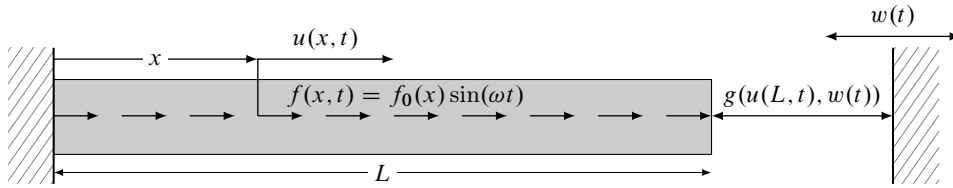


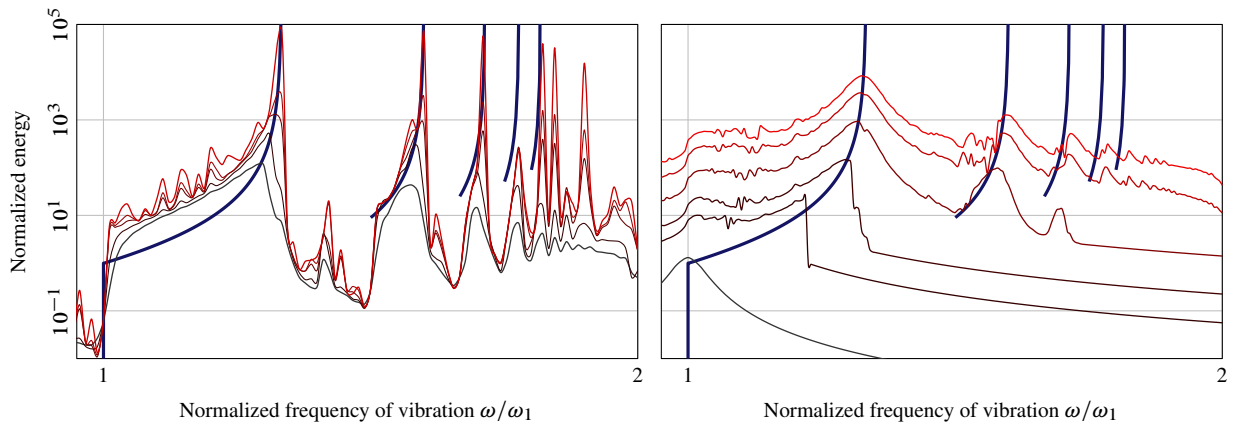
Figure 19: Elastic bar excited by a distributed harmonic force and/or a moving rigid wall.

The first tested configuration is $f_0 = 0$ and $w_0 \neq 0$. The total energy of the steady-state solution averaged over one forcing period for increasing frequencies of excitation and various dampings is shown in Figs. 20(a), 21(a) and 22(a) for a positive, zero and negative initial gap respectively.

In the frequency ranges where NSM branches do not exist, the WFEM could not find periodic steady-states. At these ranges, quasiperiodic or chaotic forced responses were observed. The calculation of steady-state for each frequency requires large computational times which complicates the construction of a detailed forced response.

The second tested configuration is $f_0 \neq 0$ and $w_0 = 0$, corresponding to the elastic bar excited by a distributed force. The results for a positive, zero and negative initial gap are depicted in Figs. 20(b), 21(b) and 22(b) respectively.

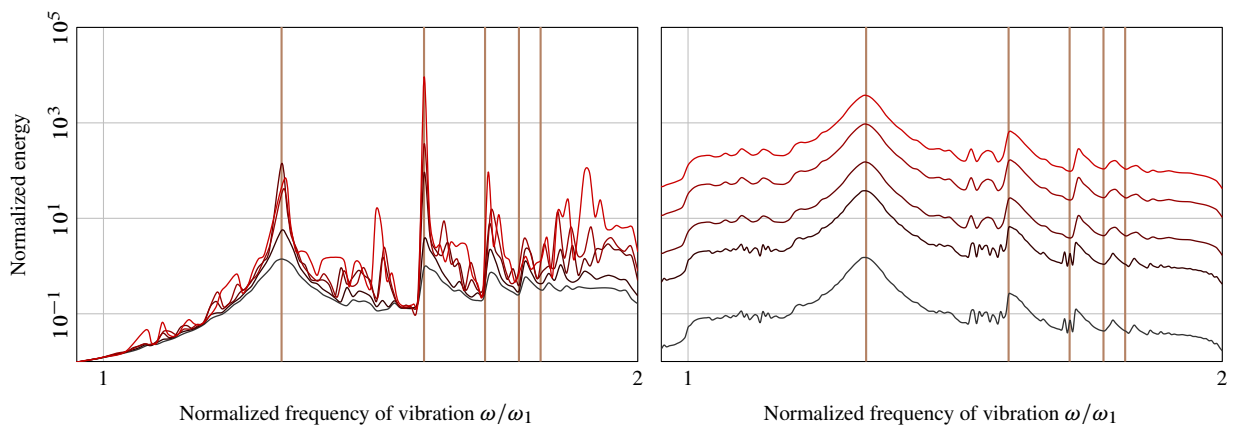
For a positive gap and high frequencies, large damping causes the bar not to close contact with the wall. This is why the forced response for large damping correspond to the linear case. Also, this is the reason why the figures for both cases differ greatly. Similarly to the first configuration, quasiperiodic and chaotic solutions are observed in the frequency intervals where NSM branches do not exist.



(a) Harmonically moving wall

(b) Harmonic distributed force

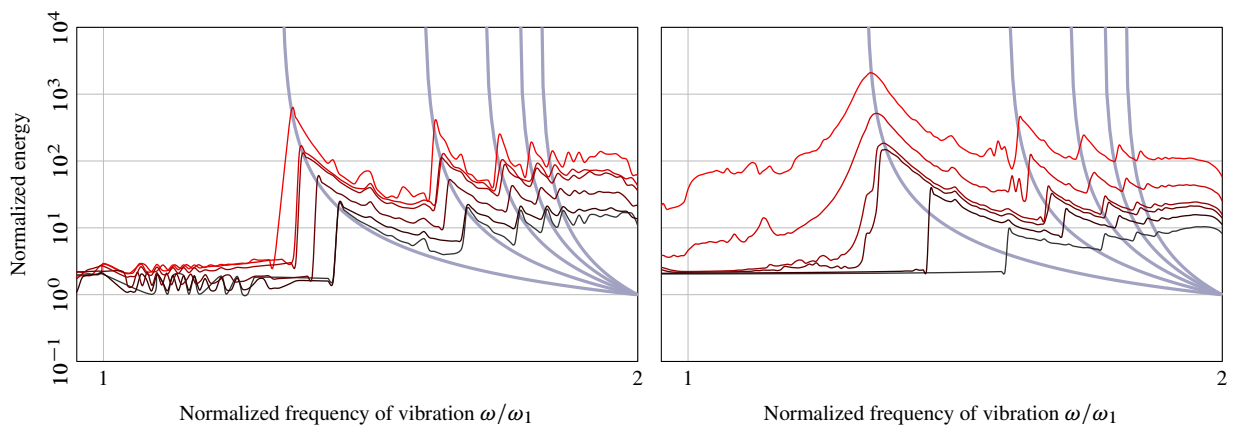
Figure 20: Periodically forced responses of the bar for various damping coefficients and $g_0 > 0$.



(a) Harmonically moving wall

(b) Harmonic distributed force

Figure 21: Periodically forced responses of the bar for various damping coefficients and $g_0 = 0$.



(a) Harmonically moving wall

(b) Harmonic distributed force

Figure 22: Periodically forced responses of the bar for various damping coefficients and $g_0 < 0$.

Most importantly, the backbone curves obtained with the nonsmooth modal analysis provide an excellent approximation of the response resonances. The internal resonances of the system cause small protuberances in the forced response that coincides with the main resonance and subharmonic backbone curves. The main advantage of the nonsmooth modal analysis is the characterization of the vibratory response without relying on very expensive numerical time-integration: via NSM as presented, the prediction of frequencies of excitation at which the system will vibrate with high energy is straightforward.

8. Conclusions

Families of periodic orbits (known as nonsmooth modes of vibration) of a finite elastic bar subject to frictionless unilateral contact are investigated in this work. Three cases were explored: unstressed ($g_0 > 0$), prestressed ($g_0 < 0$) and zero initial gap ($g_0 = 0$). The computation of periodic solutions was achieved using the Wave Finite Element Method (WFEM), chosen because it preserves energy and does not present numerical dispersion. This method consists in discretizing simultaneously in time and space the governing dynamic equations, resulting in a simple matrix form. The problem of finding periodic solutions was formulated as finding a vector in the kernel of a matrix supplemented by complementarity condition. The presented methodology can be adapted to multiple contact phases per period or to systems coupled by unilateral contact conditions. However, it is limited for one-dimensional problems with a single point of contact on the contact boundary.

It is shown that the elastic bar with unilateral contact has a rich dynamical behavior leading to sub-harmonic resonances and internal resonances. Similar results are already reported in the literature [10, 9]. However, the proposed methodology does not regularize the contact conditions. In this work, the unilateral contact conditions are treated as a switch between Dirichlet and Neumann-type boundary conditions when contact is activated: free–fixed BC (no contact) to fixed–fixed BC (contact). The found nonlinear periodic solutions lying on a NSM are combinations of traveling waves with discontinuous wave fronts, as opposed to their linear counterpart (without contact conditions) which are standing harmonic waves. Also, the behavior of the NSM depends on the gap: hardening branches for $g_0 > 0$, softening branches for $g_0 < 0$ and discrete spectrum for $g_0 = 0$. The frequency ranges at which NSM branches exist are conjectured.

Forced responses are also accurately predicted by the nonsmooth modal analysis using WFEM. The proposed approach is potentially useful for performing fatigue analyses in experimental investigations and mechanical design.

Quasi-closed form solutions can also be extracted from the provided results. They could act as benchmark solutions for researchers designing advanced numerical schemes in unilateral contact dynamics. NSM stability and the role of coexisting periodic solutions (same energy and frequency) needs to be further explored. Extension of the proposed approach to multidimensional settings with several points of contact is a remarkable challenge as the non-dispersive and energy-preserving properties of the WFEM in the one-dimensional context will then be lost.

Acknowledgments

CY gratefully acknowledges the financial support of SENESCYT (Government of Ecuador) and MEDA (McGill University) Fellowships. AT and ML acknowledge the financial support of the NSERC Discovery and FQRNT Nouveaux Chercheurs programs.

References

- [1] Peter Wriggers, Computational Contact Mechanics, Springer, 2006, [doi:10.1007/978-3-540-32609-0].
- [2] Karl Graff, Wave Motion in Elastic Solids, Dover, 1975.
- [3] David Doyen, Alexandre Ern and Serge Piperno, Time-integration schemes for the finite element dynamic Signorini problem, SIAM Journal of Scientific Computing 33 (1) (2011) 223–249, [hal-00440128].
- [4] Vincent Acary, Energy conservation and dissipation properties of time-integration methods for nonsmooth elastodynamics with contact, ZAMM-Journal of Applied Mathematics and Mechanics 96 (5) (2016) 585–603, [hal-01235240].
- [5] Singiresu Rao, Vibration of Continuous Systems, Wiley, 2007, [doi:10.1002/9780470117866].
- [6] Gaëtan Kerschen, Maxime Peeters, Jean-Claude Golinval and Alexander Vakakis, Nonlinear normal modes, Part I: A useful framework for the structural dynamicist, Mechanical Systems and Signal Processing 23 (1) (2009) 170–194, [hal-01357931].
- [7] Steven Shaw and Christophe Pierre, Normal modes of vibration for non-linear continuous systems, Journal of Sound and Vibration 169 (3) (1994) 319–347, [hal-01471098].
- [8] Vincent Acary and Bernard Brogliato, Numerical Methods for Nonsmooth Dynamical Systems, Springer, 2008, [inria-00423530].
- [9] Vladimir Babitsky, Theory of Vibro-Impact Systems and Applications, Springer, 2013, [doi:10.1007/978-3-540-69635-3].

- [10] El Hadi Moussi, Sergio Bellizzi, Bruno Cochelin and Ionel Nistor, Nonlinear normal modes of a two degrees-of-freedom piecewise linear system, *Mechanical Systems and Signal Processing* 64-65 (2015) 266–281, [[hal-01160325](#)].
- [11] Mostafa Attar, Ali Karrech and Klaus Regenauer-Lieb, Non-linear modal analysis of structural components subjected to unilateral constraints, *Journal of Sound and Vibration* 389 (2017) 380–410, [[doi:10.1016/j.jsv.2016.11.012](#)].
- [12] Denis Laxalde and Mathias Legrand, Nonlinear modal analysis of mechanical systems with frictionless contact interfaces, *Computational Mechanics* 47 (4) (2011) 469–478, [[hal-00492775](#)].
- [13] Mathias Legrand, Stéphane Junca and Sokly Heng, Nonsmooth modal analysis of a N-degree-of-freedom system undergoing a purely elastic impact law, *Communications in Nonlinear Science and Numerical Simulation* 45 (2017) 190–219, [[hal-01185980](#)].
- [14] Anders Thorin, Pierre Delezoide and Mathias Legrand, Non-smooth modal analysis of piecewise-linear impact oscillators, Preprint (2016) [[hal-01298983](#)].
- [15] Houari Khenous, Patrick Laborde and Yves Renard, Mass redistribution method for finite element contact problems in elastodynamics, *European Journal of Mechanics-A/Solids* 27 (5) (2009) 918, [[hal-00582045](#)].
- [16] Tod Laursen and Vikas Chawla, Design of energy conserving algorithms for frictionless dynamics contact problems, *International Journal for Numerical Methods in Engineering* 40 (5) (1997) 863–886, [[hal-01435617](#)].
- [17] Francisco Armero and Eva Petocz, Formulation and analysis of conserving algorithms for frictionless dynamic contact/impact problems, *Computer Methods in Applied Mechanics and Engineering* 158 (3–4) (1998) 269–300, [[hal-01435615](#)].
- [18] Boris Shorr, *The Wave Finite Element Method*, Springer, 2004, [[doi:10.1007/978-3-540-44579-1](#)].
- [19] Sergei Godunov, A difference method for numerical calculation of discontinuous solutions of the equations of hydrodynamics, *Matematicheskii Sbornik* 47(89) (3) (1959) 271–306.
- [20] Carlos Yoong, Anders Thorin and Mathias Legrand, The Wave Finite Element Method applied to a one-dimensional linear elastodynamic problem with unilateral constraints, in: *Proceedings of the 11th International Conference on Multibody Systems, Nonlinear Dynamics, and Control. International Design Engineering Technical Conferences & Computers and Information in Engineering Conference*, no. DETC2015-46919, Boston, USA, 2015, [[hal-01194922](#)].
- [21] Michelle Schatzman and Michel Bercovier, Numerical approximation of a wave equation with unilateral constraints, *Mathematics of Computation* 53 (187) (1989) 55–79, [[hal-01295436](#)].
- [22] Julian Davis, *Mathematics of Wave Propagation*, Princeton University Press, 2000.
- [23] Yves Renard, The singular dynamic method for constrained second order hyperbolic equations: Application to dynamic contact problems, *Journal of Computational and Applied Mathematics* 234 (3) (2010) 906–923, [[hal-01461799](#)].
- [24] Anders Thorin, Mathias Legrand and Stéphane Junca, Nonsmooth modal analysis: Investigation of a 2-dof spring-mass system subject to an elastic impact law, in: *Proceedings of the 11th International Conference on Multibody Systems, Nonlinear Dynamics, and Control. International Design Engineering Technical Conferences & Computers and Information in Engineering Conference*, no. DETC2015-46796, Boston, USA, 2015, [[hal-01185973](#)].
- [25] Uri Ascher, Robert Mattheij and Robert Russell, *Numerical solution of boundary value problems for ordinary differential equations*, SIAM, 1994, [[doi:10.1137/1.9781611971231](#)].
- [26] Walter Lacarbonara, Giuseppe Rega and Ali Nayfeh, Resonant non-linear normal modes. Part I: Analytical treatment for structural one-dimensional systems, *International Journal of Non-Linear Mechanics* 38 (6) (2003) 851–872, [[hal-01403851](#)].
- [27] Alberto Bressan, *Hyperbolic Systems of Conservation Laws: The One-Dimensional Cauchy Problem*, Oxford University Press, 2000.
- [28] Constantine Dafermos, *Hyperbolic Conservation Laws in Continuum Physics*, Springer, 2010, [[doi:10.1007/978-3-642-04048-1](#)].
- [29] Randall LeVeque, *Finite Volume Methods for Hyperbolic Problems*, Cambridge University Press, 2002, [[doi:10.1017/CBO9780511791253](#)].
- [30] Randall LeVeque, Finite-volume methods for non-linear elasticity in heterogeneous media, *International Journal for Numerical Methods in Fluids* 40 (1-2) (2002) 93–104, [[hal-01471101](#)].
- [31] Joel Smoller, *Shock Waves and Reaction-Diffusion Equations*, Springer, 1994, [[doi:10.1007/978-1-4612-0873-0](#)].

- [32] Eleuterio Toro, *Godunov Methods: Theory and Application*, Springer, 2001, [doi:10.1007/978-1-4615-0663-8].
- [33] Bradley Lucier, Error bounds for the methods of Glimm, Godunov and LeVeque, *SIAM Journal on Numerical Analysis* 22 (6) (1985) 1074–1081, [hal-01435616].
- [34] Christian Claudel and Alexandre Bayen, Solutions to switched hamilton-jacobi equations and conservation laws using hybrid components, in: *Proceedings of 11th International Workshop on Hybrid Systems: Computation and Control*, Vol. 4981 of *Lecture Notes in Computer Science*, Springer, St Louis, USA, 2008, pp. 101–115, [hal-01471102].

Appendix A. Description of the Wave Finite Element Method

In this section, the Wave Finite Element Method (WFEM) [18], introduced by Shorr for the simulation of shock wave propagation in solids, is thoroughly described.

Appendix A.1. Hyperbolic system of conservation laws

The local equation Eq. (1) can be written as a system of two first order partial differential equations in terms of the velocities $v(x, t)$ and stresses $\sigma(x, t)$

$$\left. \begin{aligned} \sigma_{,t} - E v_{,x} &= 0 \\ \rho v_{,t} - \sigma_{,x} &= 0 \end{aligned} \right\}, \quad \forall x \in]0; L[, \quad \forall t > 0 \quad (\text{A.1})$$

where $(\bullet)_{,t}$ is the derivation in time and $(\bullet)_{,x}$ is the derivation in space of quantity (\bullet) [27]. Recall that axial strains $\varepsilon = u_{,x}$ must not correspond to material inter-penetration, which translates into $u_{,x} > -1$, see section 2. By posing² $\mathbf{q} = [\sigma \ v]^\top$, Eq. (A.1) can be recast as

$$\mathbf{q}_{,t} + \mathbf{B}\mathbf{q}_{,x} = \mathbf{0} \quad \text{where} \quad \mathbf{B} = \begin{bmatrix} 0 & -E \\ -1/\rho & 0 \end{bmatrix}. \quad (\text{A.2})$$

The eigenvalues of matrix \mathbf{B} are $\lambda_1 = -\sqrt{E/\rho}$ and $\lambda_2 = \sqrt{E/\rho}$, coinciding with the algebraic propagation velocity of the elastic wave: positive and negative for the two waves propagating in opposite directions. Since both eigenvalues are distinct and real, Eq. (A.2) is also referred to as a *hyperbolic system of conservation laws* [27].

Equation (A.2) involves time and space derivatives of \mathbf{q} . However, observing that $\mathbf{q}_{,t} + \mathbf{B}\mathbf{q}_{,x} = \mathbf{0}$ is a local form of the conservation law of \mathbf{q} (implying $\mathbf{q}(\cdot, t)$ can only change due to fluxes at the boundaries) corresponding to the following integral form

$$\frac{d}{dt} \left(\int_{x_1}^{x_2} \mathbf{q}(x, t) dx \right) = \mathbf{B}(\mathbf{q}(x_1, t) - \mathbf{q}(x_2, t)), \quad (\text{A.3})$$

it appears that the condition on the smoothness of \mathbf{q} is no longer required. Therefore, \mathbf{q} is allowed to exhibit discontinuities in time and space [28].

Appendix A.2. Discretization

The WFEM consists in dividing the spatial and temporal domain into grid cells of equal size and keeping track of an approximation to the integral of \mathbf{q} within every single cell. As depicted in Fig. A.23, the bar is discretized using a uniform grid of N cells. Each i th cell, denoted by C_i , is delimited by the interval

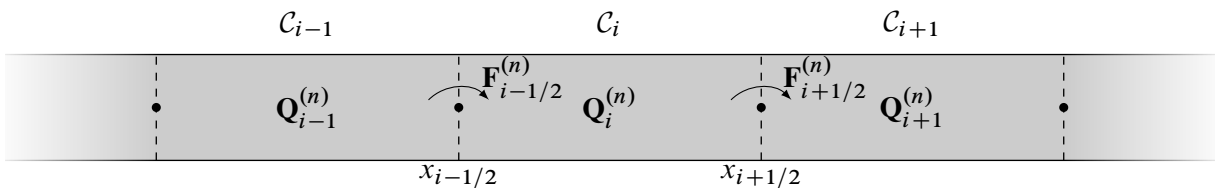


Figure A.23: Discretization of the spatial domain in grid cells at time t_n .

²For readability purposes, the transpose signs within brackets are dropped in the definitions of vectors and $\mathbf{q} = [\sigma^\top \ v^\top]^\top$ is replaced by $\mathbf{q} = [\sigma \ v]^\top$, for instance.

$(x_{i-1/2}, x_{i+1/2})$. Similarly, time is discretized into intervals of equal length $\Delta t = t_{n+1} - t_n$. The average of $\mathbf{q}(\cdot, t)$, over the i th cell at time t_n is

$$\mathbf{Q}_i^{(n)} = \frac{1}{\Delta x} \int_{x_{i-1/2}}^{x_{i+1/2}} \mathbf{q}(x, t_n) dx = \frac{1}{\Delta x} \int_{C_i} \mathbf{q}(x, t_n) dx \quad (\text{A.4})$$

where $\Delta x = x_{i+1/2} - x_{i-1/2}$ is the length of cell i . The integral form of conservation law (A.3) applied to cell C_i reads

$$\frac{d}{dt} \int_{C_i} \mathbf{q}(x, t) dx = \mathbf{B}(\mathbf{q}(x_{i-1/2}, t) - \mathbf{q}(x_{i+1/2}, t)). \quad (\text{A.5})$$

This expression is now employed to develop an explicit time-stepping algorithm where $\mathbf{Q}_i^{(n+1)}$ is approximated by a function of $\mathbf{Q}_i^{(n)}$. Equation (A.5) is integrated between t_n and t_{n+1} yielding

$$\int_{C_i} (\mathbf{q}(x, t_{n+1}) - \mathbf{q}(x, t_n)) dx = \int_{t_n}^{t_{n+1}} (\mathbf{B}(\mathbf{q}(x_{i-1/2}, t) - \mathbf{q}(x_{i+1/2}, t))) dt. \quad (\text{A.6})$$

Rearranging and dividing by Δx leads to

$$\frac{1}{\Delta x} \int_{C_i} \mathbf{q}(x, t_{n+1}) dx = \frac{1}{\Delta x} \left(\int_{C_i} \mathbf{q}(x, t_n) dx - \int_{t_n}^{t_{n+1}} \mathbf{B}\mathbf{q}(x_{i+1/2}, t) dt + \int_{t_n}^{t_{n+1}} \mathbf{B}\mathbf{q}(x_{i-1/2}, t) dt \right). \quad (\text{A.7})$$

This equation describes how the cell average should be updated within a time step in order to satisfy the conservation of \mathbf{q} . In general, the two integrals involving $\mathbf{B}\mathbf{q}$ on the right-hand side of the equation cannot be evaluated exactly. Following [29], we pose

$$\mathbf{F}_{i\pm 1/2}^{(n)} \approx \frac{1}{\Delta t} \int_{t_n}^{t_{n+1}} \mathbf{B}\mathbf{q}(x_{i\pm 1/2}, t) dt \quad (\text{A.8})$$

and Eq. (A.7) simply becomes

$$\mathbf{Q}_i^{(n+1)} = \mathbf{Q}_i^{(n)} - \frac{\Delta t}{\Delta x} (\mathbf{F}_{i+1/2}^{(n)} - \mathbf{F}_{i-1/2}^{(n)}). \quad (\text{A.9})$$

The next subsection is dedicated to the computation of $\mathbf{F}_{i\pm 1/2}^{(n)}$, which are the time-averaged fluxes at $x = x_{i\pm 1/2}$.

Appendix A.3. Approximation of the time-averaged fluxes

To approximate the fluxes in the interfaces defined by Eq. (A.8), the state $\mathbf{q}(x, t_n)$ at time t_n is assumed to be a piecewise constant function defined for all x , constructed from the cell averages $\mathbf{Q}_i^{(n)}$ as depicted in Fig. A.24. This piecewise reconstruction of the function $\mathbf{q}(x, t_n)$ is identical to the *Godunov's approach* widely employed in computational fluid dynamics [30]. A suitable approximation of the flux $\mathbf{F}_{i+1/2}^{(n)}$ can be

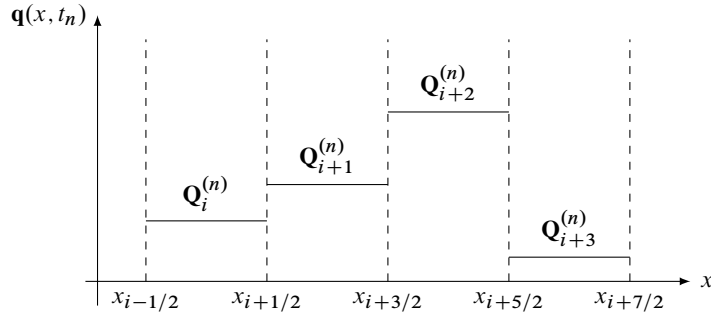


Figure A.24: Reconstruction of function $\mathbf{q}(x, t_n)$ from the average fluxes $\mathbf{Q}_i^{(n)}$.

obtained by solving the problem, either numerically or exactly, of the conservation law Eq. (A.2) together with the following discontinuous conditions at time t_n [30]:

$$\sigma(x, t_n) = \begin{cases} \sigma_i^{(n)} & \text{if } x \leq x_{i+1/2} \\ \sigma_{i+1}^{(n)} & \text{if } x > x_{i+1/2} \end{cases} \quad \text{and} \quad v(x, t_n) = \begin{cases} v_i^{(n)} & \text{if } x \leq x_{i+1/2} \\ v_{i+1}^{(n)} & \text{if } x > x_{i+1/2} \end{cases} \quad (\text{A.10})$$

which constitutes a *Riemann problem* centered at $x_{i+1/2}$ between cells \mathcal{C}_i and \mathcal{C}_{i+1} [30]. The solution to this Riemann problem consists of two shock waves propagating along the characteristic lines $x = \pm ct$, one moving to the left into cell \mathcal{C}_i and one moving to the right into cell \mathcal{C}_{i+1} as depicted in a space-time plot in Fig. A.25. The shock wave traveling to the left, indicated by \mathcal{W}_1 , propagates at velocity s_1 and connects the state $\mathbf{Q}_i^{(n)}$ and the interior state \mathbf{Q}_i^* generated by such shock wave. Moreover, the solution $t \mapsto \mathbf{q}(x_{i+1/2}, t)$ is constant over the time interval $[t_n, t_{n+1}]$.

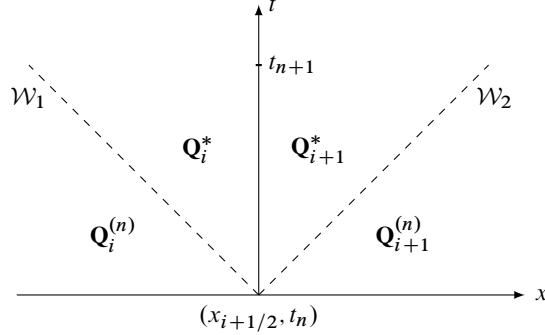


Figure A.25: Structure of the solution to the Riemann problem depicted in a space-time plot.

The *Rankine-Hugoniot jump condition* is proven to hold across any propagating discontinuity [31] which can be written for the left wave \mathcal{W}_1 propagating at velocity s_1 and the right wave \mathcal{W}_2 propagating at velocity s_2 :

$$\begin{aligned} \mathcal{W}_1 \rightarrow & \begin{cases} s_1(\sigma_i^* - \sigma_i^{(n)}) = -E(v_i^* - v_i^{(n)}), \\ \rho s_1(v_i^* - v_i^{(n)}) = -(\sigma_i^* - \sigma_i^{(n)}) \end{cases} \\ \mathcal{W}_2 \rightarrow & \begin{cases} s_2(\sigma_{i+1}^{(n)} - \sigma_{i+1}^*) = -E(v_{i+1}^{(n)} - v_{i+1}^*), \\ \rho s_2(v_{i+1}^{(n)} - v_{i+1}^*) = -(\sigma_{i+1}^{(n)} - \sigma_{i+1}^*). \end{cases} \end{aligned} \quad (\text{A.11})$$

Because of material continuity, cells \mathcal{C}_i and \mathcal{C}_{i+1} cannot separate. This requires that the interior states must be equal across the material interface, $\mathbf{Q}_{i+1/2}^* = \mathbf{Q}_{i+1}^* = \mathbf{Q}_i^*$. By knowing that the shock speeds $s_1 = -s_2 = -\sqrt{E/\rho} = -c$ are known and constants, the intermediate state is approximated with $\mathbf{q}(x_{i+1/2}, t) \approx \mathbf{Q}_{i+1/2}^*$ such that $t_n \leq t \leq t_{n+1}$ and can be calculated from Eq. (A.11):

$$\mathbf{Q}_{i+1/2}^* = \begin{bmatrix} \sigma_{i+1/2}^* \\ v_{i+1/2}^* \end{bmatrix} = \frac{1}{2} \begin{bmatrix} \sigma_{i+1}^{(n)} + \sigma_i^{(n)} + \rho c(v_{i+1}^{(n)} - v_i^{(n)}) \\ v_{i+1}^{(n)} + v_i^{(n)} + \frac{1}{\rho c}(\sigma_{i+1}^{(n)} - \sigma_i^{(n)}) \end{bmatrix}. \quad (\text{A.12})$$

Equation (A.12) is regarded as the exact solution of the Riemann problem involving linear elastodynamics [29]. The flux approximation in Eq. (A.8) can be calculated with the solution of a Riemann problem at the cell interface as follows:

$$\mathbf{F}_{i+1/2}^{(n)} \approx \frac{\mathbf{B}}{\Delta t} \int_{t_n}^{t_{n+1}} \mathbf{Q}_{i+1/2}^* dt \approx \mathbf{B} \mathbf{Q}_{i+1/2}^* \quad (\text{A.13})$$

In a nonlinear framework, the Riemann problem should be approximated numerically by the so-called Riemann solvers [32]. The linearity of the problem of interest simplifies the approximation of the fluxes between cell interfaces.

Appendix A.4. Formulation for inner grid cells

Introducing the approximation of the flux (Eq. (A.13)) in Eq. (A.9), the following numerical scheme comes:

$$\mathbf{Q}_i^{(n+1)} = \mathbf{Q}_i^{(n)} - \frac{\Delta t}{\Delta x} (\mathbf{B} \mathbf{q}_{i+1/2}^* - \mathbf{B} \mathbf{q}_{i-1/2}^*). \quad (\text{A.14})$$

Equation (A.14) describes the evolution in time of the states of the grid cells \mathcal{C}_i . This subsection provides the formulation for the inner cells, where $i = 2, \dots, N-1$. The boundary cells \mathcal{C}_1 and \mathcal{C}_N require a different

treatment provided in the next subsection. Expressing the flux approximation, employing Eq. (A.13) on the right side of an inner cell yields

$$\mathbf{Bq}_{i+1/2}^* = \frac{1}{2} \begin{bmatrix} -E(v_{i+1}^{(n)} + v_i^{(n)} + \frac{1}{\rho c}(\sigma_{i+1}^{(n)} - \sigma_i^{(n)})) \\ -\frac{1}{\rho}(\sigma_{i+1}^{(n)} + \sigma_i^{(n)} + \rho c(v_{i+1}^{(n)} - v_i^{(n)})) \end{bmatrix}. \quad (\text{A.15})$$

Performing the same operation on the left side of the cell reads

$$\mathbf{Bq}_{i-1/2}^* = \frac{1}{2} \begin{bmatrix} -E(v_i^{(n)} + v_{i-1}^{(n)} + \frac{1}{\rho c}(\sigma_i^{(n)} - \sigma_{i-1}^{(n)})) \\ -\frac{1}{\rho}(\sigma_i^{(n)} + \sigma_{i-1}^{(n)} + \rho c(v_i^{(n)} - v_{i-1}^{(n)})) \end{bmatrix}. \quad (\text{A.16})$$

Accordingly, the total flux within an inner cell is the quantity $\mathbf{Bq}_{i+1/2}^* - \mathbf{Bq}_{i-1/2}^*$ which, when substituted into Eq. (A.14) yields

$$\begin{bmatrix} \sigma_i^{(n+1)} \\ v_i^{(n+1)} \end{bmatrix} = \begin{bmatrix} \sigma_i^{(n)} \\ v_i^{(n)} \end{bmatrix} + \frac{\Delta t}{2\Delta x} \begin{bmatrix} E(v_{i+1}^{(n)} - v_{i-1}^{(n)}) + c(\sigma_{i+1}^{(n)} - 2\sigma_i^{(n)} + \sigma_{i-1}^{(n)}) \\ \frac{1}{\rho c}(\sigma_{i+1}^{(n)} - \sigma_{i-1}^{(n)}) + c(v_{i+1}^{(n)} - 2v_i^{(n)} + v_{i-1}^{(n)}) \end{bmatrix}. \quad (\text{A.17})$$

Since the exact solution of a Riemann problem is being used, WFEM incorporates an appropriate time-step $\Delta t = \Delta x/c$. Then, the values of the stress and velocity of inner grid cell C_i at time t_{n+1} are calculated as

$$\begin{bmatrix} \sigma_i^{(n+1)} \\ v_i^{(n+1)} \end{bmatrix} = \frac{1}{2} \begin{bmatrix} \sigma_{i+1}^{(n)} + \sigma_{i-1}^{(n)} + \rho c(v_{i+1}^{(n)} - v_{i-1}^{(n)}) \\ v_{i+1}^{(n)} + v_{i-1}^{(n)} + \frac{1}{\rho c}(\sigma_{i+1}^{(n)} - \sigma_{i-1}^{(n)}) \end{bmatrix}. \quad (\text{A.18})$$

The latter strong assumption is suitable only for 1D elastodynamics problems, since the wave velocity and the direction of the propagation is known. Also, such assumption enforces energy conservation and eliminates numerical dissipation [18]. In the multidimensional framework, even though the waves velocities are known, the waves could propagate in various direction throughout the physical domain.

Equation (A.18) provides the main equation of the WFEM and characterizes how the average value $\mathbf{Q}_i^{(n)}$ of \mathbf{q} in an inner cell C_i is updated at each time step. As required by the local conservation law (A.3) resulting from the absence of body forces, the evolution of the state of the inner cells depends only on the values of the adjacent cells. WFEM can be seen as the transference of the whole information embedded in cell C_i to its adjacent cells at each time step. Employing the latter approach to obtain the evolution of cell states, involving discontinuities such as shock and rarefaction waves, is well known by the Fluid Mechanics community employing Finite Volume Methods [30].

Appendix A.5. Formulation for boundary grid cells

To compute the state of the boundary grid cells, the computational domain is extended by including additional cells on both boundaries, known as *ghost cells* [29], whose average values depend on the boundary conditions. This concept is taken from the Finite Volume Methods. Figure A.26 depicts ghost cells for a system discretized using N cells.



Figure A.26: Computational space domain with ghost cells.

Equation (A.18) can then be used to update the average value on the boundary cells, which have now become *inner* cells. Only a single ghost cell is required at each boundary because the computation of the average value depends only on the states of the adjacent cells. For instance, the fixed–free elastic bar without the complementarity conditions of contact satisfies the two boundary conditions $u(0, t) = v(0, t) = 0$ and $Eu_{,x}(L, t) = \sigma(L, t) = 0$. These conditions are used to define the average values within the ghost cells as follows:

$$\text{at ghost cell } C_0: \begin{cases} \sigma_0 = \sigma_1 \\ v_0 = -v_1, \end{cases} \quad \text{and at ghost cell } C_{N+1}: \begin{cases} \sigma_{N+1} = -\sigma_N \\ v_{N+1} = v_N. \end{cases} \quad (\text{A.19})$$

Such average values coincide with the theory of reflection of elastic waves from fixed and free boundaries [2], which states that stress waves reflect from a fixed boundary with the same sign and from a free boundary with the changed sign; similarly, velocity waves reflect from a fixed boundary with an opposite sign and from a free boundary with the same sign. The evolution of the average values of the boundary cells, \mathcal{C}_1 and \mathcal{C}_N , can be calculated by introducing the average values of Eq. (A.19) into Eq. (A.18), yielding for \mathcal{C}_1

$$\mathbf{Q}_1^{(n+1)} = \begin{bmatrix} \sigma_1^{(n+1)} \\ v_1^{(n+1)} \end{bmatrix} = \frac{1}{2} \begin{bmatrix} \sigma_2^{(n)} + \sigma_1^{(n)} + \rho c (v_2^{(n)} + v_1^{(n)}) \\ v_2^{(n)} - v_1^{(n)} + \frac{1}{\rho c} (\sigma_2^{(n)} - \sigma_1^{(n)}) \end{bmatrix} \quad (\text{A.20})$$

and for \mathcal{C}_N

$$\mathbf{Q}_N^{(n+1)} = \begin{bmatrix} \sigma_N^{(n+1)} \\ v_N^{(n+1)} \end{bmatrix} = \frac{1}{2} \begin{bmatrix} \sigma_{N-1}^{(n)} - \sigma_N^{(n)} + \rho c (v_N^{(n)} + v_{N-1}^{(n)}) \\ v_N^{(n)} + v_{N-1}^{(n)} - \frac{1}{\rho c} (\sigma_N^{(n)} + \sigma_{N-1}^{(n)}) \end{bmatrix}. \quad (\text{A.21})$$

Appendix A.6. WFEM generic algorithm

Altogether, the previous derivations lead to a set of discrete equations that describe how the average values of stress and velocity stacked in \mathbf{q} is updated in time for each cell. The different steps are summarized in Algorithm 1. Using $\Delta t = \Delta x/c$ it computes, in the framework of linear elastodynamics, the propagation at

Algorithm 1: WFEM Computation procedure

Input: number of elements N , total number of steps n_T , boundary conditions, initial conditions, density ρ , wave velocity c
for $n = 0$ to n_T [Time Loop] **do**
 Update time instant: $t_n = n\Delta t$;
 Compute stress and velocity at cell \mathcal{C}_1 using Eq. (A.20);
 for $i = 2$ to $N - 1$ [Cell Loop] **do**
 Compute stress and velocity at cell \mathcal{C}_i using Eq. (A.18);
 end
 Compute stress and velocity at cell \mathcal{C}_N using Eq. (A.21);
end
Output: stresses, velocities at instants t_0, \dots, t_{n_T}

finite speed c of a wave and accounts for the reflection conditions at the boundaries. By definition of Δt , the CFL condition $\Delta t \leq \Delta x/c$ is always satisfied, so the method is always stable [29, 33]. Additionally, because the global error is proportional to the discretization steps, the WFEM is first-order accurate both in space and time [18].

Appendix A.7. Matrix formulation

Similar to other numerical methods applied on linear systems, the WFEM can be rewritten in a convenient matrix form which facilitates the process of finding nonsmooth modes of vibration. More specifically, the state vector of the system $\mathbf{Q}^{(n)} = [\mathbf{Q}_1^{(n)} \dots \mathbf{Q}_N^{(n)}]^\top \in \mathbb{R}^{2N}$ at time t_n satisfies the identity

$$\mathbf{Q}^{(n)} = \mathbf{A}\mathbf{Q}^{(n-1)}, \quad \forall n \geq 1 \quad (\text{A.22})$$

and $\mathbf{Q}^{(0)}$ is the initial state. The matrix \mathbf{A} gathers stiffness and inertial terms as well as the type of boundary conditions. It is now derived for the fixed–free BC. In a matrix form, Eq. (A.18), which governs the evolution of inner cells, reads

$$\begin{bmatrix} \sigma_i^{(n+1)} \\ v_i^{(n+1)} \end{bmatrix} = \frac{1}{2} \begin{bmatrix} 1 & 0 & 1 & -\rho c & 0 & \rho c \\ -\frac{1}{\rho c} & 0 & \frac{1}{\rho c} & 1 & 0 & 1 \end{bmatrix} \begin{bmatrix} \sigma_{i-1}^{(n)} & \sigma_i^{(n)} & \sigma_{i+1}^{(n)} & v_{i-1}^{(n)} & v_i^{(n)} & v_{i+1}^{(n)} \end{bmatrix}^\top. \quad (\text{A.23})$$

For the boundary cells in Eqs (A.20) and (A.21), the matrix form follows as

$$\begin{bmatrix} \sigma_1^{(n+1)} \\ v_1^{(n+1)} \end{bmatrix} = \frac{1}{2} \begin{bmatrix} 1 & 1 & \rho c & \rho c \\ -\frac{1}{\rho c} & \frac{1}{\rho c} & -1 & 1 \end{bmatrix} \begin{bmatrix} \sigma_1^{(n)} & \sigma_2^{(n)} & v_1^{(n)} & v_2^{(n)} \end{bmatrix}^\top \quad (\text{A.24})$$

and

$$\begin{bmatrix} \sigma_N^{(n+1)} \\ v_N^{(n+1)} \end{bmatrix} = \frac{1}{2} \begin{bmatrix} 1 & -1 & \rho c & \rho c \\ -\frac{1}{\rho c} & -\frac{1}{\rho c} & 1 & 1 \end{bmatrix} \begin{bmatrix} \sigma_{N-1}^{(n)} & \sigma_N^{(n)} & v_{N-1}^{(n)} & v_N^{(n)} \end{bmatrix}^T. \quad (\text{A.25})$$

Then the block matrix $\mathbf{A} \in \mathbb{R}^{2N \times 2N}$ can be constructed using four $N \times N$ matrices $\mathbf{A}_1, \mathbf{A}_2, \mathbf{A}_3, \mathbf{A}_4$ whose expression can be derived from

$$\mathbf{A}_g(a, b, c, d) = \frac{1}{2} \begin{bmatrix} a & b & 0 & \dots & 0 & 0 & 0 \\ c & 0 & b & & 0 & 0 & 0 \\ 0 & c & 0 & & 0 & 0 & 0 \\ \vdots & & \ddots & \ddots & \ddots & & \vdots \\ 0 & 0 & 0 & & 0 & b & 0 \\ 0 & 0 & 0 & & c & 0 & b \\ 0 & 0 & 0 & \dots & 0 & c & d \end{bmatrix} \quad (\text{A.26})$$

using the identities $\mathbf{A}_1 = \mathbf{A}_g(-1, 1, 1, 1)$, $\mathbf{A}_2 = \rho c \mathbf{A}_g(-1, 1, -1, -1)$, $\mathbf{A}_3 = \mathbf{A}_g(1, 1, -1, 1)/\rho c$, and $\mathbf{A}_4 = \mathbf{A}_g(1, 1, 1, -1)$. Then, block matrix \mathbf{A} is written as

$$\mathbf{A} = \begin{bmatrix} \mathbf{A}_1 & \mathbf{A}_2 \\ \mathbf{A}_3 & \mathbf{A}_4 \end{bmatrix}. \quad (\text{A.27})$$

Another matrix \mathbf{A} can be constructed in the same way for the fixed–fixed BC. Finally, the unknown $\mathbf{Q}^{(n)}$ can be directly expressed in terms of the initial conditions $\mathbf{Q}^{(0)}$ from Eq. (A.22) by

$$\mathbf{Q}^{(n)} = \mathbf{A}^n \mathbf{Q}^{(0)} \quad (\text{A.28})$$

where \mathbf{A}^n is known for each type of BC.

Appendix B. Treatment of unilateral contact in WFEM

The unilateral contact constraints involved in the formulation are enforced using the concept of *floating boundary conditions* [18] which can be regarded as a conditional switch between fixed–free and fixed–fixed boundary conditions [34] when a penetration is detected during a time iteration, as illustrated in Fig. B.27. In the continuous framework, these two boundary conditions are

$$\begin{aligned} \text{free–fixed BC (inactive contact)} & \quad u(0, t) = v(0, t) = 0, \quad Eu_{,x}(L, t) = \sigma(L, t) = 0 \\ \text{fixed–fixed BC (active contact)} & \quad u(0, t) = v(0, t) = 0, \quad u(L, t) = g_0 \rightarrow v(L, t) = 0. \end{aligned} \quad (\text{B.1})$$

The gap function $g(u(L, t))$, which is a function of the displacement $u(L, t)$ but not an explicit function of t , is discretized in time to calculate a possible penetration of the bar as

$$g^{(n)} = g_0 - u_{N+1/2}^{(n)} \quad (\text{B.2})$$

where $u_{N+1/2}^{(n)}$ is the displacement of the contacting interface which can be calculated by numerically integrating the velocity $v_{N+1/2}$ of the bar at $x_{N+1/2}$. This equality is used at each time step to check whether contact is active during the next iteration: if $g^{(n)} > 0$, a free boundary condition is enforced while if $g^{(n)} \leq 0$, a fixed boundary condition is considered via the change of matrix \mathbf{A} .

Based on the theory of reflection of elastic waves from boundaries [2], the state of the ghost cell \mathcal{C}_{N+1} is updated as follows

- Active contact [$g^{(n)} \leq 0$]

$$\begin{cases} \sigma_{N+1} = \sigma_N \\ v_{N+1} = -v_N \end{cases} \quad (\text{B.3})$$

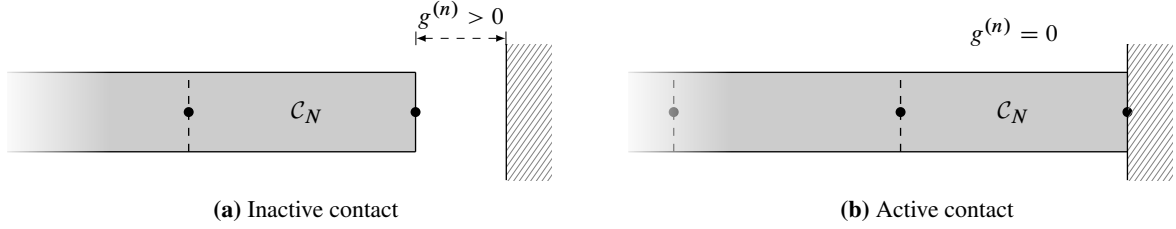


Figure B.27: Conditional switch for contact treatment in WFEM

- Inactive contact [$g^{(n)} > 0$]

$$\begin{cases} \sigma_{N+1} = -\sigma_N \\ v_{N+1} = v_N \end{cases} \quad (\text{B.4})$$

Equation (A.18) is subsequently used to calculate the evolution of the average values inside the boundary cell C_N , as detailed in section Appendix A.5. Additionally, the contact force $r^{(n)}$ is calculated by employing Eq. (A.12):

$$r^{(n)} = \mathcal{S}(\sigma_N^{(n)} - \rho c v_N^{(n)}). \quad (\text{B.5})$$

The sign of this quantity is tracked to locate the time of release, when the bar returns to free condition at $x = L$. Algorithm 1 is modified to include the floating boundary conditions as described in Algorithm 2.

Algorithm 2: Computation procedure with unilateral contact conditions

Input: number of elements N , number of steps n_T , boundary and initial conditions, density ρ , wave velocity c
for $n = 0$ to n_T [*Time Loop*] **do**

 Discrete time instant, $t_n = n\Delta t$;

 Compute stress and velocity at cell C_1 using Eq. (A.20);

for $i = 2$ to $N - 1$ [*Element Loop*] **do**

 | Compute stress and velocity at cell C_i using Eq. (A.18);

end

 — floating boundary conditions —

if $g^{(n)} = 0$ **then**

 | Switch to fixed boundary condition at $x_{N+1/2}$;

 | Compute contact stress $r^{(n)}$ using Eq. (B.5);

if $r^{(n)} > 0$ **then**

 | Switch to free boundary condition at $x_{N+1/2}$;

 | Compute gap $g^{(n+1)}$;

 | Compute stress and velocity at cell C_N using Eq. (A.21);

else

 | Keep fixed boundary condition at $x_{N+1/2}$;

 | Compute stress and velocity at cell C_N using Eq. (A.21);

end

else

 | Keep free boundary condition at $x_{N+1/2}$;

 | Compute gap $g^{(n+1)}$ and stress and velocity at cell C_N using Eq. (A.21);

end

 — end of floating boundary conditions —

end

Output: stresses, velocities, contact force at instants t_0, \dots, t_{n_T}

From the matrix formulation of the WFEM in Eq. (A.22), two matrices \mathbf{A} shall then be distinguished: \mathbf{A}_f for the fixed–free condition (no contact) and \mathbf{A}_c for fixed–fixed condition (contact). Both matrices embed the same stiffness and inertial terms of the system of interest; the only unshared information are the boundary conditions. To summarize, the developed WFEM with floating boundary conditions is a numerically conservative and stable scheme able to properly propagate shock waves induced by a switch in the boundary conditions, the latter being governed by complementarity constraints.